

A Quantum Monte Carlo algorithm for non-local corrections to the Dynamical Mean-Field Approximation

M. Jarrell, Th. Maier, C. Huscroft, and S. Moukouri
University of Cincinnati, Cincinnati OH 45221, USA

We present the algorithmic details of the dynamical cluster approximation (DCA), with a quantum Monte Carlo (QMC) method used to solve the effective cluster problem. The DCA is a fully-causal approach which systematically restores non-local correlations to the dynamical mean field approximation (DMFA) while preserving the lattice symmetries. The DCA becomes exact for an infinite cluster size, while reducing to the DMFA for a cluster size of unity. We present a generalization of the Hirsch-Fye QMC algorithm for the solution of the embedded cluster problem. We use the two-dimensional Hubbard model to illustrate the performance of the DCA technique. At half-filling, we show that the DCA drives the spurious finite-temperature antiferromagnetic transition found in the DMFA slowly towards zero temperature as the cluster size increases, in conformity with the Mermin-Wagner theorem. Moreover, we find that there is a finite temperature metal to insulator transition which persists into the weak-coupling regime. This suggests that the magnetism of the model is Heisenberg like for all non-zero interactions. Away from half-filling, we find that the sign problem that arises in QMC simulations is significantly less severe in the context of DCA. Hence, we were able to obtain good statistics for small clusters. For these clusters, the DCA results show evidence of non-Fermi liquid behavior and superconductivity near half-filling.

I. INTRODUCTION

One of the most active subfields in condensed matter theory is the development of new algorithms to simulate the many-body problem. This interest is motivated by various physical phenomena, including high temperature superconductivity, magnetism, heavy fermions and the rich phenomenology occurring in quasi-one dimensional compounds. In the last few years, important progress has been made. Well-controlled results have been obtained by exact diagonalization and quantum Monte Carlo methods (QMC) [1]. However, these algorithms suffer from a common limitation in that the number of degrees of freedom grows rapidly with the lattice size. As a consequence, the calculations are restricted to relatively small systems. In most cases, the limited size of the system prohibits the study of the low-energy physics of these models.

Recently, another route to quantum simulations has been proposed. Following Metzner and Vollhardt [2] and Müller-Hartmann [3] who showed that in the limit of infinite dimensions, the many-body problem becomes purely local, a mapping to a self-consistent Anderson impurity

problem was performed [4,5]. The availability of many techniques to solve the Anderson impurity Hamiltonian has led to a dramatic burst of activity. However, when applied to systems in two or three dimensions this self-consistent approximation, referred to as the dynamical mean field approximation (DMFA), displays some limitations. Due to its local nature, the DMFA neglects spatial fluctuations which are essential when the order parameter is non-local, or when short-ranged spin correlations are present.

An acceptable theory which systematically incorporates non-local corrections to the DMFA is needed. It must be able to account for fluctuations in the local environment in a self-consistent way, become exact in the limit of large cluster sizes, and recover the DMFA when the cluster size equals one. It must be easily implementable numerically and preserve the translational and point-group symmetries of the lattice. Finally, it should be fully causal so that the single-particle Green function and self energy are analytic in the upper half plane. There have been several attempts to formulate theories which satisfy these requirements, but all fail in some significant way [6].

In recent publications [7–9], the dynamical cluster approximation (DCA) has been proposed as an extension to the DMFA which satisfies all these criteria. The DCA is built in close analogy with the DMFA. In the DCA, the lattice problem is mapped to a self-consistently embedded finite-sized cluster, instead of a single impurity as in the DMFA. The key idea of the DCA is to use the irreducible quantities (self energy, irreducible vertices) of the embedded cluster as an approximation for the corresponding lattice quantities. These irreducible quantities are then applied to construct the lattice reducible quantities such as the Green function or susceptibilities in the different channels. The cluster problem generated by the DCA may be solved by using a variety of techniques including the Quantum Monte Carlo (QMC) method [10], the Fluctuation Exchange (FLEX) approximation [11] or the Non-Crossing Approximation (NCA) [12].

The QMC method, and the Hirsch-Fye algorithm [10] in particular, is the most reliable of these techniques. The Hirsch-Fye algorithm was originally designed for the treatment of few-impurity problems. Hence, it has been widely applied to the Kondo problem [10] and also to solve the impurity problem of the DMFA. For embedded cluster problems, this algorithm shows a mild sign problem, compared to that encountered in previous finite-sized simulations, presumably due to the coupling to the host. Thus, we are able to perform simulations at sig-

nificantly lower temperatures than with other available techniques. However, in order to study a meaningful set of clusters of different sizes, it is necessary to use massively parallel computers.

Throughout this paper, we will use the two-dimensional Hubbard model on a simple square lattice as an example. Its Hamiltonian is

$$H = - \sum_{\mathbf{ij}} t_{\mathbf{ij}} (c_{\mathbf{i}\sigma}^\dagger c_{\mathbf{j}\sigma} + \text{h.c.}) + \epsilon \sum_{\mathbf{i}\sigma} n_{\mathbf{i}\sigma} + U \sum_{\mathbf{i}} (n_{\mathbf{i}\uparrow} - 1/2)(n_{\mathbf{i}\downarrow} - 1/2) \quad (1)$$

where $t_{\mathbf{ij}}$ is the matrix of hopping integrals, $c_{\mathbf{i}\sigma}^{(\dagger)}$ is the annihilation (creation) operator for electrons on lattice site \mathbf{i} with spin σ , and U the intraatomic repulsion. We will take $\mu = 0$ and vary the orbital energy ϵ to fix the filling. The model has a long history and is still the subject of an intensive research in relation with the high-temperature superconductivity, the non-Fermi liquid phenomenon, the metal to insulator transition and magnetism in various physical systems dominated by strong correlations. Some short accounts [13,14] of the DCA applied to this model have been recently published but without a full description of the details of the algorithm and numerical subtleties. It is the purpose of this paper to present the full account of the DCA-QMC technique. A typical DCA algorithm using the QMC technique as the cluster solver is made of three main blocks: the self-consistent loop, the analysis block and the analytical continuation block. The self-consistent loop is the most important of the three blocks; it is devoted to the mapping of the lattice to the cluster (coarse-graining) and to the solution of the cluster problem by the QMC method. In the analysis block, cluster Green functions obtained from the QMC method are transformed to lattice Green functions following the procedure described in section III. The last block is devoted to the computation of the lattice real frequency quantities from the analytical continuation of the corresponding QMC imaginary-time quantities by the maximum entropy method (MEM). [15]

This paper is organized as follows. In the next section, we review the dynamical mean field approximation. In Sec. III, we review the DCA formalism in which the lattice problem is mapped to a self-consistently embedded periodic cluster, and discuss the relationship between the cluster and the lattice. In this section we describe how different lattice Green functions can be obtained from the cluster quantities. In Sec. IV, we derive a modified form of the Hirsch-Fye QMC algorithm, which may be used to solve the effective cluster problem. We also discuss the conditioning and optimization of a variety of one and two-particle measurements. In Sec. V, we discuss the DCA algorithm. In Sec. VI, we will show our results for the two-dimensional Hubbard model. Comparisons between the DCA and the results of finite-sized simulations will be made in order to outline the complementarity of the

two techniques which has been discussed in earlier publications [13,14,16]. At half-filling we discuss the occurrence of antiferromagnetism and the metal to insulator transition. Away from half-filling, we show the signature of a non-Fermi liquid behavior and superconductivity for small clusters for which the negative sign problem is mild so that good statistics can be obtained at low temperatures. Finally, in Sec. VII, we draw the conclusions on the present work and discuss future applications of the DCA to various physical problems.

II. THE DYNAMICAL MEAN-FIELD APPROXIMATION

The DCA algorithm is constructed in analogy with the DMFA. The DMFA is a local approximation which was used by various authors in perturbative calculations as a simplification of the k-summations which render the problem intractable [17,18]. But it was after the work of Metzner and Vollhardt [2] and Müller-Hartmann [3] who showed that this approximation becomes exact in the limit of infinite dimension that it received extensive attention during the last decade. In this approximation, one neglects the spatial dependence of the self-energy, retaining only its variation with time. Please see the reviews by Pruschke *et al* [4] and Georges *et al* [5] for a more extensive treatment. In this section, we will show that it is possible to re-interpret the DMFA as a coarse graining approximation, and then review its derivation.

The DMFA consists of mapping the original lattice problem to a self-consistent impurity problem. As illustrated in Fig. 1 for a two-dimensional lattice, this is equivalent to averaging the Green functions used to calculate the irreducible diagrammatic insertions over the Brillouin zone. An important consequence of this averaging is that the self-energy and the irreducible vertices of the lattice are independent of the momentum. Hence, they are those of the impurity.

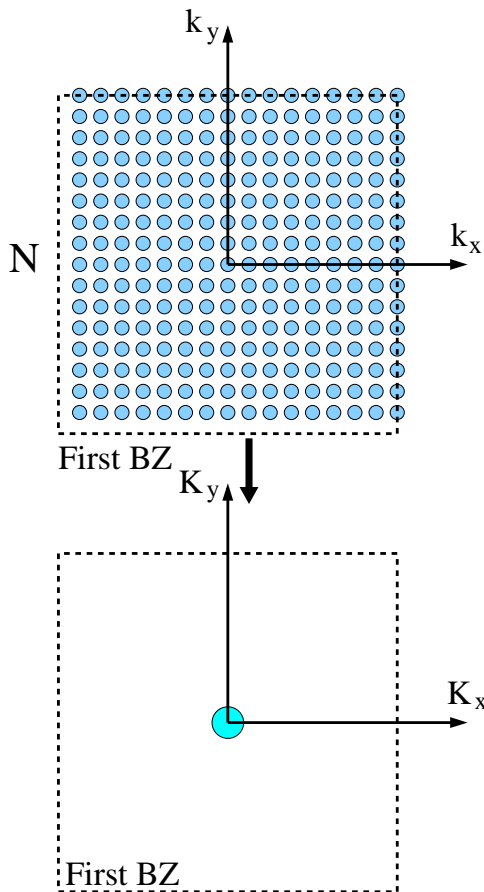


FIG. 1. A single step illustration of coarse-graining in the DMFA: all lattice propagators used to calculate the self energy are averaged over the points in the first Brillouin zone (top). This effectively maps the lattice problem to a single point in reciprocal space (bottom). Since the real space and reciprocal space of a single-site cluster are equivalent, this mapping takes the lattice problem to one of an impurity embedded within a host.

Müller-Hartmann [3] showed that this coarse-graining becomes exact in the limit of infinite-dimensions. For Hubbard-like models, the properties of the bare vertex are completely characterized by the Laue function Δ which expresses the momentum conservation at each vertex. In a conventional diagrammatic approach

$$\Delta(\mathbf{k}_1, \mathbf{k}_2, \mathbf{k}_3, \mathbf{k}_4) = \sum_{\mathbf{r}} \exp[i\mathbf{r} \cdot (\mathbf{k}_1 + \mathbf{k}_2 - \mathbf{k}_3 - \mathbf{k}_4)] \quad (2)$$

$$= N\delta_{\mathbf{k}_1 + \mathbf{k}_2, \mathbf{k}_3 + \mathbf{k}_4}$$

where \mathbf{k}_1 and \mathbf{k}_2 (\mathbf{k}_3 and \mathbf{k}_4) are the momenta entering (leaving) each vertex through its legs of G . However as the dimensionality $D \rightarrow \infty$ Müller-Hartmann showed that the Laue function reduces to [3]

$$\Delta_{D \rightarrow \infty}(\mathbf{k}_1, \mathbf{k}_2, \mathbf{k}_3, \mathbf{k}_4) = 1 + \mathcal{O}(1/D) \quad . \quad (3)$$

The DMFA assumes the same Laue function, $\Delta_{DMFA}(\mathbf{k}_1, \mathbf{k}_2, \mathbf{k}_3, \mathbf{k}_4) = 1$, even in the context of finite dimensions. Thus, the conservation of momentum

at internal vertices is neglected. Therefore we may freely sum over the internal momentum labels of each Green function leg. This leads to a collapse of the momentum dependent contributions and only local terms remain.

This argument may then be applied to the free energy functional. As discussed in many-body texts [19], the additional free energy due to an interaction may be described by a sum over all closed connected graphs. These graphs may be further separated into compact and non-compact graphs. The compact graphs, which comprise the generating functional Φ , consist of the sum over all single-particle irreducible graphs. The remaining graphs, comprise the non-compact part of the free energy. In the infinite-dimensional limit, Φ consists of only local graphs, with non-local corrections of order $1/D$. However, for the non-compact parts of the free energy, non-local corrections are of order one, so the local approximation applies only to Φ . Thus, whereas irreducible quantities such as the self energy are momentum independent, the corresponding reducible quantities such as the lattice Green function are momentum dependent.

The perturbative series for Σ in the local approximation is identical to that of the corresponding impurity model. However in order to avoid overcounting the local self-energy $\Sigma(i\omega_n)$, it is necessary to exclude $\Sigma(i\omega_n)$, $i\omega_n = (2n + 1)\pi T$ is the Matsubara frequency, from the bare local propagator \mathcal{G} . $\mathcal{G}(i\omega_n)^{-1} = G(i\omega_n)^{-1} + \Sigma(i\omega_n)$ where $G(i\omega_n)$ is the full local Green function. Hence, in the local approximation, the Hubbard model has the same diagrammatic expansion as an Anderson impurity with a bare local propagator $\mathcal{G}(i\omega_n; \Sigma)$ which is determined self-consistently.

An algorithm constructed from this approximation is the following: (i) An initial guess for $\Sigma(i\omega_n)$ is chosen (usually from perturbation theory). (ii) $\Sigma(i\omega_n)$ is used to calculate the corresponding local Green function

$$G(i\omega_n) = \int d\eta \frac{\rho^0(\eta)}{i\omega_n - \eta - \epsilon - \Sigma(i\omega_n)}, \quad (4)$$

where ρ^0 is the non-interacting density of states. (iii) Starting from $G(i\omega_n)$ and $\Sigma(i\omega_n)$ used in the second step, the host Green function $\mathcal{G}(i\omega_n)^{-1} = G(i\omega_n)^{-1} + \Sigma(i\omega_n)$ is calculated which serves as bare Green function of the impurity model. (iv) starting with $\mathcal{G}(i\omega_n)$, the local Green function $G(i\omega_n)$ is obtained using the Quantum Monte Carlo method (or another technique). (v) Using the QMC output for the cluster Green function $G(i\omega_n)$ and the host Green function $\mathcal{G}(i\omega_n)$ from the third step, a new $\Sigma(i\omega_n) = \mathcal{G}(i\omega_n)^{-1} - G(i\omega_n)^{-1}$ is calculated, which is then used in step (ii) to reinitialize the process. Steps (ii) - (v) are repeated until convergence is reached. In step (iv) the QMC algorithm of Hirsch and Fye [10] may be used to compute the local Green function $G(\tau)$ or other physical quantities in imaginary time. Local dynamical quantities are then calculated by analytically continuing the corresponding imaginary-time quantities using the Maximum-Entropy Method (MEM) [15].

III. THE DYNAMICAL CLUSTER APPROXIMATION

In this section, we will review the formalism which leads to the dynamical cluster approximation. Here, we first motivate the fundamental idea of the DCA which is coarse-graining, we then describe the mapping to an effective cluster problem and discuss the relationship between the cluster and lattice at the one and two-particle level.

A. Coarse-Graining

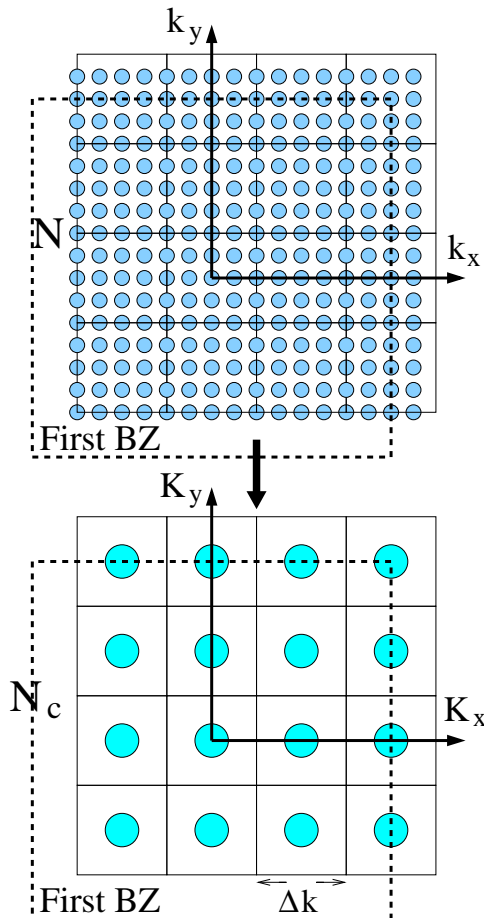


FIG. 2. A single step illustration of coarse-graining in the DCA: all lattice propagators used to calculate the self energy are first averaged over the points within each cell in the Brillouin zone (top), mapping the lattice problem to a small cluster defined by the centers of the cells embedded within a host (bottom).

Like the DMFA, the DCA may be intuitively motivated with a coarse-graining transformation. In the DMFA, the propagators used to calculate Φ and its derivatives were coarse-grained over the entire Brillouin zone, leading to local (momentum independent) irreducible quantities. In

the DCA, we wish to relax this condition, and systematically restore momentum conservation and non-local corrections. Thus, in the DCA, the reciprocal space of the lattice (Fig. 2) which contains N points is divided into N_c cells of identical linear size Δk . The coarse-graining transformation is set by averaging the Green function within each cell. If $N_c = 1$ the original lattice problem is mapped to an impurity problem (DMFA). If N_c is larger than one, then non-local corrections of length $\approx \pi/\Delta k$ to the DMFA are introduced. Provided that the propagators are sufficiently weakly momentum dependent, this is a good approximation. If N_c is chosen to be small, the cluster problem can be solved using conventional techniques such as QMC, NCA or FLEX. This averaging process also establishes a relationship between the systems of size N and N_c . A simple and unique choice which will be discussed in Sec. IIIB is to equate the irreducible quantities (self energy, irreducible vertices) of the cluster to those in the lattice.

B. A diagrammatic derivation

This coarse graining procedure and the relationship of the DCA to the DMFA is illustrated by a microscopic diagrammatic derivation of the DCA.

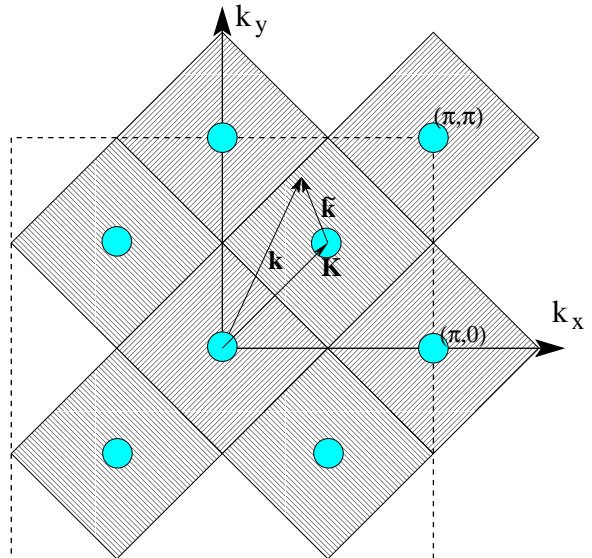


FIG. 3. Coarse-graining cells for $N_c = 8$ (differentiated by alternating fill patterns) that partition the first Brillouin Zone (dashed line). Each cell is centered on a cluster momentum \mathbf{K} (filled circles). To construct the DCA cluster, we map a generic momentum in the zone such as \mathbf{k} to the nearest cluster point $\mathbf{K} = \mathbf{M}(\mathbf{k})$ so that $\bar{\mathbf{k}} = \mathbf{k} - \mathbf{K}$ remains in the cell around \mathbf{K} .

The DCA systematically restores the momentum conservation at internal vertices relinquished by the DMFA. The Brillouin-zone is divided into $N_c = L^D$ cells of size $\Delta k = 2\pi/L$ (c.f. Fig. 3 for $N_c = 8$). Each cell is rep-

resented by a cluster momentum \mathbf{K} in the center of the cell. We require that momentum conservation is (partially) observed for momentum transfers between cells, i.e., for momentum transfers larger than Δk , but neglected for momentum transfers within a cell, i.e., less than Δk . This requirement can be established by using the Laue function [8]

$$\Delta_{DCA}(\mathbf{k}_1, \mathbf{k}_2, \mathbf{k}_3, \mathbf{k}_4) = N_c \delta_{\mathbf{M}(\mathbf{k}_1)+\mathbf{M}(\mathbf{k}_2), \mathbf{M}(\mathbf{k}_3)+\mathbf{M}(\mathbf{k}_4)} \quad , \quad (5)$$

where $\mathbf{M}(\mathbf{k})$ is a function which maps \mathbf{k} onto the momentum label \mathbf{K} of the cell containing \mathbf{k} (see, Fig. 3). This choice for the Laue function systematically interpolates between the exact result, Eq. 2, which it recovers when $N_c \rightarrow N$ and the DMFA result, Eq. 3, which it recovers when $N_c = 1$. With this choice of the Laue function the momenta of each internal leg may be freely summed over the cell.

This is illustrated for the second-order term in the generating functional in Fig. 4. Each internal leg $G(\mathbf{k})$ in a diagram is replaced by the coarse-grained Green function $\bar{G}(\mathbf{M}(\mathbf{k}))$, defined by

$$\bar{G}(\mathbf{K}) \equiv \frac{N_c}{N} \sum_{\tilde{\mathbf{k}}} G(\mathbf{K} + \tilde{\mathbf{k}}) \quad , \quad (6)$$

where N is the number of points of the lattice, N_c is the number of cluster \mathbf{K} points, and the $\tilde{\mathbf{k}}$ summation runs over the momenta of the cell about the cluster momentum \mathbf{K} (see, Fig. 3). The diagrammatic sequences for the generating functional and its derivatives are unchanged; however, the complexity of the problem is greatly reduced since $N_c \ll N$.

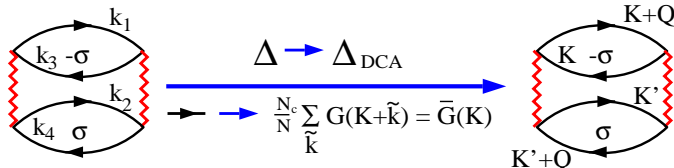


FIG. 4. A second-order term in the generating functional of the Hubbard model. Here the undulating line represents the interaction U , and on the LHS (RHS) the solid line the lattice (coarse-grained) single-particle Green functions. When the DCA Laue function is used to describe momentum conservation at the internal vertices, the momenta collapse onto the cluster momenta and each lattice Green function is replaced by the coarse-grained result.

As with the DMFA, the coarse-graining approximation will be applied to only the compact part of the free energy, Φ , and its derivatives. This is justified by the fact that there is no need to coarse-grain the remaining terms in the free energy. Formally, we have justified this elsewhere by exploring the Δk -dependence of the compact and non-compact parts of the free energy [20]. The generating functional is the sum over all of the closed

connected compact diagrams, such as the one shown in Fig. 4. The corresponding DCA estimate for the free energy is

$$F_{DCA} = -k_B T (\Phi_c - \text{tr} [\Sigma_\sigma \mathbf{G}_\sigma] - \text{tr} \ln [-\mathbf{G}_\sigma]) \quad (7)$$

where Φ_c is the cluster generating functional. The trace indicates summation over frequency, momentum and spin. F_{DCA} is stationary with respect to \mathbf{G}_σ ,

$$\frac{-1}{k_B T} \frac{\delta F_{DCA}}{\delta G_\sigma(\mathbf{k})} = \Sigma_{c\sigma}(\mathbf{M}(\mathbf{k})) - \Sigma_\sigma(\mathbf{k}) = 0, \quad (8)$$

which means that $\Sigma(\mathbf{k}) = \Sigma_{c\sigma}(\mathbf{M}(\mathbf{k}))$ is the proper approximation for the lattice self energy corresponding to Φ_c . The corresponding lattice single-particle propagator is then given by

$$G(\mathbf{k}, z) = \frac{1}{z - \epsilon_{\mathbf{k}} - \epsilon - \Sigma_c(\mathbf{M}(\mathbf{k}), z)}. \quad (9)$$

A variety of techniques may be used to sum the cluster diagrams in order to calculate Σ_c and the vertex functions Γ_c . In the past, we have used QMC [13], the non-crossing approximation [9] or the Fluctuation-Exchange approximation. Here, we will use the QMC technique which we will detail in Sec. IV. Since QMC is systematically exact; i.e. it effectively sums all diagrams to all orders, care must be taken when defining the initial Green function (the solid lines in Fig. 4) to avoid overcounting diagrams on the cluster. For example, to fourth order and higher in perturbation theory for the self energy, non-trivial self energy corrections enter in the diagrammatic expansion for the cluster self energy of the Hubbard model. To avoid overcounting these contributions, we must first subtract off the self energy corrections on the cluster from the Green function line used to calculate Σ_c and its functional derivatives. This cluster-excluded Green function is given by

$$\frac{1}{\mathcal{G}(\mathbf{K}, z)} = \frac{1}{\bar{G}(\mathbf{K}, z)} + \Sigma_c(\mathbf{K}, z) \quad (10)$$

which is the coarse-grained Green function with correlations on the cluster excluded. Since $\Sigma_c(\mathbf{K}, z)$ is not known *a priori*, it must be determined self-consistently, starting from an initial guess, usually from perturbation theory. This guess is used to calculate \bar{G} from Eq. 6. $\mathcal{G}(\mathbf{K}, z)$ is then calculated with Eq. 10, and it is used to initialize the QMC calculation. The QMC estimate for the cluster self energy is then used to calculate a new estimate for $\bar{G}(\mathbf{K})$ using Eq. 6. The corresponding $\mathcal{G}(\mathbf{K})$ is used to reinitialize the procedure which continues until $G_c = \bar{G}$ and the self energy converges to the desired accuracy.

One of the difficulties encountered in earlier attempts to include non-local corrections to the DMFA was that these methods were not causal [21,22]. The spectral weight was not conserved and the imaginary parts of the

one-particle retarded Green functions and self-energies were not negative definite as required by causality. The DCA algorithm presented in this subsection does not present these problems. This algorithm is fully causal as shown by Hettler *et al.* [8]. They analyze the different steps of the self-consistent loop and found that none of them breaks the causality of the Green functions. Starting from the QMC block, one can see that if the input \mathcal{G} is causal, since the QMC algorithm is essentially exact, the output G_c will also be causal. Then the corresponding $\Sigma_c(\mathbf{K}, i\omega_n)$ is causal. This in turn ensures that the coarse-grained Green function $\bar{G}(\mathbf{K}, i\omega_n)$ also fulfills causality. The only non-trivial operation which may break causality is the calculation of $\mathcal{G}(\mathbf{K}, i\omega_n)$. Hettler *et al.* used a geometric proof to show that even this part of the loop respects causality.

In the remainder of this section, we will give further details about the DCA formalism, and discuss the relationship between the cluster and the lattice problems. Below, we will discuss the steps necessary to choose the coarse-graining cells and ensure that symmetries of the lattice are preserved.

C. Selecting the Coarse-Graining cells

As we will see in Sec. IV the solution of the cluster problem using the quantum Monte Carlo method though is a great simplification over the original lattice problem is still a formidable task. The reason is that the self-consistent nature of the cluster problem forces us to adopt the Hirsch-Fye algorithm. While this algorithm is very efficient for few impurity problems, it becomes slow even for a cluster of a modest size. Therefore, in order to study the size dependence of physical quantities we adopt various cluster tilings of the lattice instead of confining ourselves to only the usual square tilings $N_c = 4, 16, 36, 64, \dots$

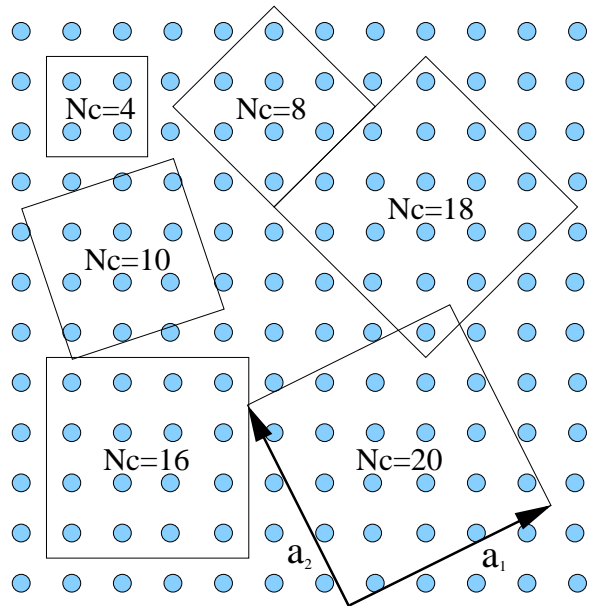


FIG. 5. Different tile sizes and orientations in real space. The tiling principle translation vectors, \mathbf{a}_1 and \mathbf{a}_2 , form two sides of each tiling square (illustrated for the $N_c = 20$ tiling). For square tile geometries, $a_{2x} = -a_{1y}$ and $a_{2y} = a_{1x}$.

When selecting the coarse-graining cells, it is important to preserve the point group symmetries of the lattice. For example, in this study, we will choose a simple square lattice. Both it and its reciprocal lattice share C_{4v} symmetry with eight point group operations. We must choose a set of coarse-graining cells which preserve the lattice symmetry. This may be done by tiling the real lattice with squares, and using the \mathbf{K} points that correspond to the reciprocal space of the tiling centers. We also will only consider tilings which contain an even number of sites, to avoid frustrating the magnetic correlations on the cluster. Square tilings with an even number of sites include $N_c = 4, 8, 10, 16, 18, 20, 26, 32, 34, 36, \dots$. The first few are illustrated in Fig. 5. The relation between the principle lattice vectors of the lattice centers, \mathbf{a}_1 and \mathbf{a}_2 , and the reciprocal lattice takes the usual form $\mathbf{g}_i = 2\pi\mathbf{a}_i/(\mathbf{a}_1 \times \mathbf{a}_2)$, with $\mathbf{K}_{nm} = n\mathbf{g}_1 + m\mathbf{g}_2$ for integer n and m . For tilings with either $a_{1x} = a_{1y}$ (corresponding to $N_c = 1, 8, 18, 32, \dots$) or one of a_{1x} or a_{1y} zero (corresponding to $N_c = 1, 4, 16, 36, \dots$), the principle reciprocal lattice vectors of the coarse-grained system either point along the same directions as the principle reciprocal lattice vectors of the real system or are rotated from them by $\pi/4$. As a result, equivalent momenta \mathbf{k} are always mapped to equivalent coarse-grained momenta \mathbf{K} . An example for $N_c = 8$ is shown in Fig. 6. However, for $N_c = 10, 20, 26, 34, \dots$, the principle reciprocal lattice vectors of the coarse-grained system do not point along a high symmetry direction of the real lattice. Since all points within a coarse-grained cell are mapped to its center \mathbf{K} , this means that these coarse-graining choices violate the point group symmetry of the real system. This is illustrated for $N_c = 10$ in Fig. 6, where the two open

dots resting at equivalent points in the real lattice, fall in inequivalent coarse-graining cells and so are mapped to inequivalent \mathbf{K} points. Thus the tilings corresponding to $N_c = 10, 20, 26, 34, \dots$ violate the point-group symmetry of the real lattice and will be avoided in this study.

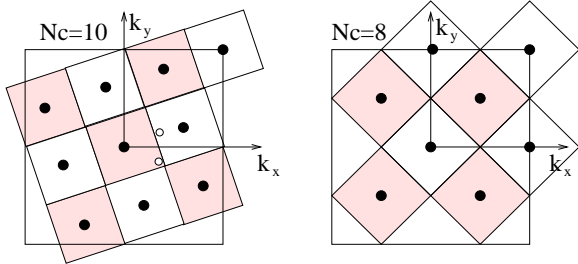


FIG. 6. The coarse graining cells for $N_c = 8$ and 10 each centered on a coarse-grained momenta \mathbf{K} represented as black filled dots. For $N_c = 8$ equivalent momenta \mathbf{k} are always mapped to equivalent coarse-grained momenta \mathbf{K} . However, this is not true for $N_c = 10$ where, for example, the two equivalent momenta shown by open dots are mapped to inequivalent coarse-grained momenta.

One should note that the coarse-graining scheme also depends strongly on dimensionality. For example, in one dimension, any cell with an even number of sites will preserve the lattice symmetry.

D. One-particle Green functions

In the DMFA, after convergence, the local Green function of the lattice is identical to that of the impurity model. Though in the DCA, the coarse-grained Green function $\tilde{G}(\mathbf{K}, i\omega_n)$ is equal to the cluster Green function $G_c(\mathbf{K}, i\omega_n)$, this quantity is not, however, used as an approximation to the true lattice Green function $G(\mathbf{K}, i\omega_n)$. The correct procedure to calculate the lattice physical quantities within the DCA is to approximate the lattice irreducible quantities with those of the cluster. The lattice reducible quantities are then deduced from the irreducible. This procedure was justified formally in Sec.III B. To obtain a physical understanding, one must first understand why reducible and irreducible quantities must be treated differently. Consider a quasiparticle propagating through the system. The screening cloud is described by the single-particle self-energy $\Sigma(\mathbf{k}, \omega)$ which itself may be considered a functional of the interaction strength U and the single-particle propagator $G(\mathbf{k}, \omega)$, $\Sigma = \Sigma[U, G]$. The different screening processes are described perturbatively by a sum of self-energy diagrams. If the size of the screening cloud r_s is short, the propagators which describe these processes need only be accurate for distances $< r_s$. From the Fourier uncertainty principle, we know that the propagators at short distances may be accurately described by a coarse sampling of the reciprocal space, with sampling rate $\Delta k = \pi/r_s$. Hence, in this case, $\Sigma[U, G]$ may be quite well approximated by

$\Sigma[U, \tilde{G}]$.

On the other hand, the phase accumulated as the particle propagates through the system is described by the Fourier transform of the single-particle Green function. Since this accumulated phase is crucial in the description of the quantum dynamics it is important that $G(r)$ remains accurate at long distances, so it should not be coarse-grained as described above. However it may be constructed from the approximate self-energy. Hence, the approximate lattice Green function is given by Eq. 9. Thus, as in the DMFA, the lattice Green function is generally more strongly momentum dependent than the corresponding self energy.

In the case of the 2D Hubbard model, non-local correlations are the most important in the parameter regime close to the quantum critical point at half filling. Away from this parameter regime r_s is thus expected to be short. Here, the above construction scheme for the approximate lattice Green function is likely to yield accurate results even for clusters of modest size. However, as the quantum critical point is approached, longer range correlations are important. As a consequence one will need to evaluate $\Sigma[U, \tilde{G}]$ on larger clusters.

E. Two-Particle Green Functions

A similar procedure is used to construct the two-particle quantities needed to determine the phase diagram or the nature of the dominant fluctuations that can eventually destroy the quasi-particle. This procedure is a generalization of the method of calculating response functions in the DMFA [23,24]. In the DCA, the introduction of the momentum dependence in the self-energy will allow one to detect some precursor effects which are absent in the DMFA; but for the actual determination of the nature of the instability, one needs to compute the response functions. These susceptibilities are thermodynamically defined as second derivatives of the free energy with respect to external fields. $\Phi_c(\mathbf{G})$ and $\Sigma_{c\sigma}$, and hence F_{DCA} depend on these fields only through G_σ and G_σ^0 . Following Baym [25] it is easy to verify that, the approximation

$$\Gamma_{\sigma, \sigma'} \approx \Gamma_{c\sigma, \sigma'} \equiv \delta \Sigma_{c\sigma} / \delta G_{\sigma'} \quad (11)$$

yields the same estimate that would be obtained from the second derivative of F_{DCA} with respect to the applied field. For example, the first derivative of the free energy with respect to a spatially homogeneous external magnetic field h is the magnetization,

$$m = \text{tr} [\sigma \mathbf{G}_\sigma]. \quad (12)$$

The susceptibility is given by the second derivative,

$$\frac{\partial m}{\partial h} = \text{tr} \left[\sigma \frac{\partial \mathbf{G}_\sigma}{\partial h} \right]. \quad (13)$$

We substitute $\mathbf{G}_\sigma = (\mathbf{G}_\sigma^{0-1} - \Sigma_{c\sigma})^{-1}$, and evaluate the derivative,

$$\frac{\partial m}{\partial h} = \text{tr} \left[\sigma \frac{\partial \mathbf{G}_\sigma}{\partial h} \right] = \text{tr} \left[\mathbf{G}_\sigma^2 \left(1 + \sigma \frac{\partial \Sigma_{c\sigma}}{\partial \mathbf{G}_{\sigma'}} \frac{\partial \mathbf{G}_{\sigma'}}{\partial h} \right) \right]. \quad (14)$$

If we identify $\chi_{\sigma,\sigma'} = \sigma \frac{\partial \mathbf{G}_{\sigma'}}{\partial h}$, and $\chi_\sigma^0 = \mathbf{G}_\sigma^2$, collect all of the terms within both traces, and sum over the cell momenta $\tilde{\mathbf{k}}$, we obtain the two-particle Dyson's equation

$$2(\bar{\chi}_{\sigma,\sigma} - \bar{\chi}_{\sigma,-\sigma}) \quad (15) \\ = 2\bar{\chi}_\sigma^0 + 2\bar{\chi}_\sigma^0 (\mathbf{\Gamma}_{c\sigma,\sigma} - \mathbf{\Gamma}_{c\sigma,-\sigma}) (\bar{\chi}_{\sigma,\sigma} - \bar{\chi}_{\sigma,-\sigma}).$$

We see that again it is the irreducible quantity, i.e. the vertex function, for which cluster and lattice correspond.

1. particle-hole

In this subsection we will provide more details about the relationship between the lattice and cluster two-particle Green functions and describe how a particle-hole susceptibility may be calculated efficiently. As a specific example, we will describe the calculation of the two-particle Green function

$$\chi_{\sigma,\sigma'}(q, k, k') = \int_0^\beta \int_0^\beta \int_0^\beta \int_0^\beta d\tau_1 d\tau_2 d\tau_3 d\tau_4 \\ \times e^{i((\omega_n + \nu)\tau_1 - \omega_n\tau_2 + \omega_n\tau_3 - (\omega_n + \nu)\tau_4)} \\ \times \langle T_\tau c_{\mathbf{k}+\mathbf{q}\sigma}^\dagger(\tau_1) c_{\mathbf{k}\sigma}(\tau_2) c_{\mathbf{k}'\sigma'}^\dagger(\tau_3) c_{\mathbf{k}'+\mathbf{q}\sigma'}(\tau_4) \rangle,$$

where we adopt the conventional notation [19] $k = (\mathbf{k}, i\omega_n)$, $k' = (\mathbf{k}, \omega'_n)$, $q = (\mathbf{q}, \nu_n)$ and T_τ is the time ordering operator.

$\chi_{\sigma,\sigma'}(q, k, k')$ and $\Gamma_{\sigma,\sigma'}(q, k, k')$ are related to each other through the Bethe-Salpeter equation:

$$\chi_{\sigma,\sigma'}(q, k, k') = \chi_{\sigma,\sigma'}^0(q, k, k') + \chi_{\sigma,\sigma''}^0(q, k, k'') \\ \times \Gamma_{\sigma'',\sigma'''}(q, k'', k''') \chi_{\sigma''',\sigma'}(q, k''', k') \quad (16)$$

where $\Gamma_{\sigma,\sigma'}(q, k, k')$ is the two-particle irreducible vertex which is the analogue of the self-energy, $\chi_{\sigma,\sigma'}^0(q, k, k'')$ is the non-interacting susceptibility constructed from a pair of fully-dressed single-particle Green functions. As usual, a summation is to be made for repeated indices.

We now make the DCA substitution $\Gamma_{\sigma,\sigma'}(\mathbf{q}, \mathbf{k}, \mathbf{k}') \rightarrow \Gamma_{c\sigma,\sigma'}(\mathbf{q}, \mathbf{M}(\mathbf{k}), \mathbf{M}(\mathbf{k}'))$ in Eq. 16 (where frequency labels have been suppressed). Note that only the bare and dressed two-particle Green functions χ depend upon the momenta $\tilde{\mathbf{k}}$ within a cell. Since χ and χ^0 in the product on the RHS of Eq. 16 share no common momentum labels, we may freely sum over the momenta $\tilde{\mathbf{k}}$ within a cell, yielding

$$\bar{\chi}_{\sigma,\sigma'}(q, K, K') = \bar{\chi}_{\sigma,\sigma'}^0(q, K, K') + \bar{\chi}_{\sigma,\sigma''}^0(q, K, K'') \\ \times \Gamma_{c\sigma'',\sigma'''}(q, K'', K''') \bar{\chi}_{\sigma''',\sigma'}(q, K''', K'). \quad (17)$$

By coarse-graining the Bethe-Salpeter equation, we have greatly reduced its complexity; each of the matrices above is sufficiently small that they may be easily manipulated using standard techniques.

In contrast with the single-particle case where the coarse-grained quantities are identical to those of the cluster, $\chi_{c\sigma,\sigma'}(q, K, K')$ is not equal to $\bar{\chi}_{\sigma,\sigma'}(q, K, K')$. This is because the self-consistency is made only at the single-particle level. Unlike the single particle case where both $\Sigma(K)$ and $\bar{G}(K)$ are directly calculated, neither $\Gamma_{\sigma,\sigma'}(q, K, K')$ nor the coarse-grained susceptibility $\bar{\chi}_{\sigma,\sigma'}(q, K, K')$ are calculated during the self-consistency. Instead, the coarse-grained non-interacting susceptibility $\bar{\chi}_{\sigma,\sigma'}^0(q, K, K')$ is calculated in a separate program after the DCA converges using the following relation

$$\bar{\chi}_{\sigma,\sigma'}^0[(\mathbf{q}, i\nu_n); (\mathbf{K}, i\omega_n); (\mathbf{K}', i\omega'_n)] = \delta_{\sigma,\sigma'} \delta_{\mathbf{K},\mathbf{K}'} \delta_{\omega_n,\omega'_n} \\ \times \frac{N_c}{N} \sum_{\tilde{\mathbf{k}}} G_\sigma(\mathbf{K} + \tilde{\mathbf{k}}, i\omega_n) G_\sigma(\mathbf{K} + \tilde{\mathbf{k}} + \mathbf{q}, i\omega_n + \nu_n) \quad (18)$$

The corresponding cluster susceptibility is calculated in the QMC process, as discussed in Sec. IV D and the vertex function is extracted by inverting the cluster two-particle Bethe-Salpeter equation

$$\chi_{c\sigma,\sigma'}(q, K, K') = \chi_{c\sigma,\sigma'}^0(q, K, K') + \chi_{c\sigma,\sigma''}^0(q, K, K'') \\ \times \Gamma_{c\sigma'',\sigma'''}(q, K'', K''') \chi_{c\sigma''',\sigma'}(q, K''', K'). \quad (19)$$

If we combine Eqs. 19 and 17, then the coarse-grained susceptibility may be obtained after elimination of $\Gamma(q, K, K')$ between the two equations. It reads

$$\bar{\chi}^{-1} = \chi_c^{-1} - \chi_c^{0-1} + \bar{\chi}^{0-1}, \quad (20)$$

where, for example, $\bar{\chi}$ is the matrix formed from $\bar{\chi}_{\sigma,\sigma'}(q, K, K')$ for fixed q . The charge (*ch*) and spin (*sp*) susceptibilities $\chi_{ch,sp}(q, T)$ are deduced from $\bar{\chi}$

$$\chi_{ch,sp}(q, T) = \frac{(k_B T)^2}{N_c^2} \sum_{KK'\sigma\sigma'} \lambda_{\sigma\sigma'} \bar{\chi}_{\sigma,\sigma'}(q, K, K') \quad (21)$$

where $\lambda_{\sigma\sigma'} = 1$ for the charge channel and $\lambda_{\sigma\sigma'} = \sigma\sigma'$ for the spin channel.

2. particle-particle

The calculation of susceptibilities in the particle-particle channel is essentially identical to the above. The exception to this rule occurs when we calculate susceptibilities for transitions to states of lower symmetry than the lattice symmetry. For example, in order to obtain the pair function of the desired symmetry (*s, p, d*), the two-particle Green function must be multiplied by the corresponding form factors $g(\mathbf{k})$ and $g(\mathbf{k}')$. In the study of the Hubbard model below, we will be particularly interested in $g(\mathbf{k}) = 1$ (*s* wave), $g(\mathbf{k}) = \cos(k_x) + \cos(k_y)$

(extended s wave) and $g(\mathbf{k}) = \cos(k_x) - \cos(k_y)$ ($d_{x^2-y^2}$ wave). These symmetries have been evoked as possible candidates for the superconducting ground state.

These factors modify the Bethe-Salpeter equations

$$g(\mathbf{k})\chi(q, k, k')g(\mathbf{k}') = g(\mathbf{k})\chi^0(q, k, k')g(\mathbf{k}') + g(\mathbf{k})\chi^0(q, k, k'') \times \Gamma(q, k'', k''') \times \chi(q, k''', k')g(\mathbf{k}') \quad (22)$$

where

$$\chi(q, k, k') = \int_0^\beta \int_0^\beta \int_0^\beta \int_0^\beta d\tau_1 d\tau_2 d\tau_3 d\tau_4 \times e^{i((\omega_n + \nu)\tau_1 - \omega_n\tau_2 + \omega_{n'}\tau_3 - (\omega_{n'} + \nu)\tau_4)} \times \langle T_\tau c_{\mathbf{k}+\mathbf{q}\sigma}^\dagger(\tau_1) c_{-\mathbf{k}-\sigma}^\dagger(\tau_2) c_{-\mathbf{k}'-\sigma}(\tau_3) c_{\mathbf{k}'+\mathbf{q}\sigma}(\tau_4) \rangle, \quad (23)$$

On the LHS, we have dropped the spin indices since we will consider only opposite-spin pairing. Eq. 22 cannot be easily solved if it is coarse-grained, since this will partially convolve $\chi(q, k, k')$ with *two* factors of g on the LHS and *one* factor on the RHS. Hence for the pairing susceptibilities, or for any situation where non-trivial form factors must be used, we use the equivalent equation involving the reducible vertex T_2 (instead of the irreducible vertex Γ)

$$g(\mathbf{k})\chi(q, k, k')g(\mathbf{k}') = g(\mathbf{k})\chi^0(q, k, k')g(\mathbf{k}') + g(\mathbf{k})\chi^0(q, k, k'') \times T_2(q, k'', k''')\chi^0(q, k''', k')g(\mathbf{k}'), \quad (24)$$

where

$$T_2(q, k, k') = \Gamma(q, k, k') + \chi^0(q, k, k'')\Gamma(q, k'', k''')\chi^0(q, k''', k') + \dots \quad (25)$$

We define

$$\Pi_{g,g}(q, k, k') = g(\mathbf{k})\chi(q, k, k')g(\mathbf{k}') \quad (26)$$

$$\Pi_{g,g}^0(q, k, k') = g(\mathbf{k})\chi^0(q, k, k')g(\mathbf{k}') \quad (27)$$

$$\Pi_g^0(q, k, k') = g(\mathbf{k})\chi^0(q, k, k'). \quad (28)$$

The remaining steps of the calculation are similar to the particle-hole case. We invert the cluster particle-particle Bethe-Salpeter equation with $g = 1$ for the cluster, in order to extract Γ_c . We then coarse-grain Eq. 25, and use Γ_c to calculate the coarse-grained $\bar{T}_2 = \Gamma_c (1 - \bar{\chi}^0 \Gamma_c)^{-1}$. We then coarse-grain Eq. 24, and use the coarse-grained \bar{T}_2 to calculate the coarse-grained $\bar{\Pi}_{g,g}$

$$\bar{\Pi}_{g,g}(q, K, K') = \bar{\Pi}_{g,g}^0(q, K, K') + \bar{\Pi}_{g,g}^0(q, K, K'')\bar{T}_2(q, K'', K''')\bar{\Pi}_{g,g}^0(q, K''', K'). \quad (29)$$

The pairing susceptibility of a desired symmetry is given by

$$P_g(q, T) = \frac{(k_B T)^2}{N_c^2} \sum_{K, K'} \bar{\Pi}_{gg}(q, K, K') \quad (30)$$

F. Local quantities

We will also need to evaluate a number of local quantities on the lattice. They include the magnetic moment, the local magnetic susceptibility, the local Green function, etc. The local cluster quantities are identical to the local lattice ones. This may be seen for example on the one-particle Green function. The coarse-grained Green function is related to the lattice Green function as follows

$$\bar{G}(\mathbf{r}, \omega) = \frac{1}{N} \sum_{\mathbf{K}, \mathbf{k}} \sum_{\mathbf{X}, \mathbf{r}'} e^{i\mathbf{K} \cdot (\mathbf{r} - \mathbf{r}')} e^{i\mathbf{k} \cdot (\mathbf{X} + \mathbf{r}')} G(\mathbf{X} + \mathbf{r}', \omega). \quad (31)$$

It is easy to see from this relation that $\bar{G}(0, \omega) = G(0, \omega)$.

IV. THE QUANTUM MONTE CARLO ALGORITHM

In this section we will derive a generalization of the Hirsch-Fye Anderson impurity algorithm suitable to simulate a Hubbard cluster embedded in a self-consistently determined host. We will then discuss the differences between this algorithm and the more familiar Blencowe-Sugar-Scalapino (BSS) algorithm [26] used to simulate finite-sized systems. Finally, we will discuss how different quantities mentioned above may be measured efficiently and how the code can be optimized.

A. Formalism

The Hirsch-Fye algorithm is an action-based technique. Therefore, knowledge of the underlying Hamiltonian is not required provided that we know the Green function for the non-interacting cluster coupled to the host, and the interacting part of the action or Hamiltonian. The interacting part is unchanged by the coarse-graining since it is purely local. It may be written in the real space as follows,

$$H_I = U \sum_{\mathbf{i}=1}^{N_c} (n_{\mathbf{i},\uparrow} - 1/2)(n_{\mathbf{i},\downarrow} - 1/2), \quad (32)$$

and the bare cluster Green function is $\mathcal{G}(\mathbf{K}, i\omega_n)$.

Given this information, the most direct way to derive this algorithm is to express the partition function as path integrals over Grassmann variables. The first step is to disentangle the interacting, H_I , and non-interacting, H_0 , parts of the Hamiltonian using a Trotter-Suzuki decomposition for the partition function. We divide the interval $[0, \beta]$ into N_l sufficiently small subintervals $\Delta\tau = \beta/N_l$ such that $\Delta\tau^2 [H_0, H_I]$ may be neglected. This leads to

$$Z = \text{Tr} e^{-\beta H} = \text{Tr} \prod_{l=1}^{N_l} e^{-\Delta\tau H} \approx \text{Tr} \prod_{l=1}^{N_l} e^{-\Delta\tau H_0} e^{-\Delta\tau H_I}. \quad (33)$$

The interacting part of the Hamiltonian may be further decoupled by mapping it to an auxiliary Ising field via a discrete Hirsch-Hubbard-Stratonovich (HHS) [27] transformation,

$$\begin{aligned} e^{-\Delta\tau H_I} &= e^{-\Delta\tau U \sum_i (n_{i\uparrow}-1/2)(n_{i\downarrow}-1/2)} \\ &= \frac{1}{2} e^{-\Delta\tau U/4} \prod_i \sum_{s_i=\pm 1} e^{\alpha s_i (n_{i\uparrow}-n_{i\downarrow})}, \end{aligned} \quad (34)$$

where $\cosh(\alpha) = e^{\Delta\tau U/2}$.

We now introduce coherent states of the operators on the cluster and in the host as the basis states and express the partition function as path integrals over the corresponding Grassmann variables $\gamma_{\mathbf{i},l,\sigma}$ and $\phi_{\mathbf{k},l,\sigma}$ defined over each N_l time slices $\tau_l = l\Delta\tau$ of the interval $[0, \beta]$ [28]. After substituting the Grassmann variables one obtains the following approximation for the partition function which becomes exact as $\Delta\tau \rightarrow 0$,

$$Z \approx \int \mathcal{D}[\gamma] \mathcal{D}[\phi] e^{-S_0[\gamma, \phi]} e^{-S_I[\gamma]}, \quad (35)$$

where $\mathcal{D}[\dots]$ symbols denote the measures of path integration over the corresponding Grassmann fields and $S_{(0)I}$ is the (non-)interacting part of the action. The interacting part of the action, becomes

$$S_I[\gamma] = - \sum_{i=1}^{N_c} \sum_{l=1}^{N_l} \sum_{\sigma} \alpha \gamma_{\mathbf{i},l,\sigma}^* \sigma s_{\mathbf{i},l} \gamma_{\mathbf{i},l-1,\sigma}. \quad (36)$$

The non-interacting parts are

$$\begin{aligned} S_0[\gamma, \phi] &= \Delta\tau \sum_{\mathbf{k},l} \left[\phi_{\mathbf{k},l,\sigma}^* \left(\frac{\phi_{\mathbf{k},l,\sigma} - \phi_{\mathbf{k},l-1,\sigma}}{\Delta\tau} \right) \right. \\ &\quad \left. + H_{host}(\phi_{\mathbf{k},l,\sigma}^*, \phi_{\mathbf{k},l-1,\sigma}) \right] \\ &+ \Delta\tau \sum_{\mathbf{i},l,\sigma} \gamma_{\mathbf{i},l,\sigma}^* \left(\frac{\gamma_{\mathbf{i},l,\sigma} - \gamma_{\mathbf{i},l-1,\sigma}}{\Delta\tau} \right) \\ &+ \Delta\tau \sum_{\mathbf{k},\mathbf{i},l,\sigma} H_{cluster}^0(\phi_{\mathbf{k},l,\sigma}^*, \phi_{\mathbf{k},l-1,\sigma}; \gamma_{\mathbf{i},l,\sigma}^*, \gamma_{\mathbf{i},l-1,\sigma}) \end{aligned} \quad (37)$$

where H_{host} , $H_{cluster}^0$ are the Hamiltonian for the host, and the non-interacting degrees of freedom on the cluster including the coupling to the host, respectively. The detailed form of both H_{host} and $H_{cluster}^0$ are unknown, due to the self-consistent renormalization of the host. However, both are purely bilinear, and may be integrated out of the action *without further approximation*.

We will first integrate out the host degrees of freedom. The partition function becomes

$$Z \propto \left[\prod_{\mathbf{k},\sigma} \det(g_{\mathbf{k},\sigma})^{-1} \right] \int \mathcal{D}[\gamma] \mathcal{D}[\phi] e^{-S_c[\gamma]} \quad (38)$$

where $g_{\mathbf{k},\sigma}$ is the Green function of the host. It remains fixed during the QMC process, and it may be disregarded

since, as we show below, we only require knowledge of the ratio of the partition functions for two different configurations of the HHS fields. Other fixed prefactors (depending upon U , $\beta \dots$) have also been disregarded in Eq. 38. S_c is the cluster action. It takes the form

$$S_c[\gamma] = \sum_{\mathbf{i},l;\mathbf{i}',l',\sigma} \gamma_{\mathbf{i},l,\sigma}^* \mathcal{G}^{-1}(\mathbf{i},l;\mathbf{i}',l') \gamma_{\mathbf{i}',l',\sigma} + S_I[\gamma] \quad (39)$$

where $\mathcal{G}(\mathbf{i},l;\mathbf{i}',l')$ is the cluster excluded (i.e. non-interacting on the cluster) Green function, defined previously. Now we will integrate out the remaining cluster Grassmann variables. The partition function then becomes

$$Z \propto Tr_{\{s_{\mathbf{i},l}\}} \prod_{\sigma} \det(G_{c\sigma;s_{\mathbf{i},l}})^{-1} \quad (40)$$

where again factors which are fixed during the QMC process have been ignored. $(G_{c\sigma;s_{\mathbf{i},l}})^{-1}$ is the inverse cluster Green function matrix with elements

$$(G_{c\sigma;s_{\mathbf{i},l}})^{-1}_{\mathbf{i},\mathbf{j},l,l'} = \delta_{\mathbf{i},\mathbf{j}} \delta_{l',l-1} \alpha \sigma s_{\mathbf{i},l}(\tau_l) + \mathcal{G}_{\mathbf{i},\mathbf{j},l,l'}^{-1}. \quad (41)$$

If we re-exponentiate the first term in the RHS of the above formula by defining $\mathcal{V}_{\sigma}(\mathbf{i},l) \equiv \alpha s_{\mathbf{i},l} \sigma$, we can write Eq. 41 in a simple matrix notation as

$$G_{c\sigma}^{-1} = \mathcal{G}^{-1} + T(e^{\mathcal{V}_{\sigma}} - 1), \quad (42)$$

where T is $\delta_{i,j} \delta_{l-1,l'}$. The matrix product $G_{c\sigma}^{-1} e^{-\mathcal{V}_{\sigma}}$ depends upon the HHS fields only along its diagonal elements. As can be seen from Eq. 37, each diagonal element of the matrices \mathcal{G}^{-1} and hence $G_{c\sigma}^{-1}$ is 1. Therefore, the inverse Green functions for two different field configurations, $\{s_{i,l}\}$ and $\{s'_{i,l}\}$, are related by

$$G_{c\sigma}'^{-1} e^{-\mathcal{V}'_{\sigma}} = G_{c\sigma}^{-1} e^{-\mathcal{V}_{\sigma}} - e^{-\mathcal{V}_{\sigma}} + e^{-\mathcal{V}'_{\sigma}}. \quad (43)$$

Or, after multiplying by $e^{\mathcal{V}'_{\sigma}}$, and collecting terms

$$G_{c\sigma}'^{-1} - G_{c\sigma}^{-1} = (G_{c\sigma}^{-1} - 1) e^{-\mathcal{V}_{\sigma}} (e^{\mathcal{V}'_{\sigma}} - e^{\mathcal{V}_{\sigma}}). \quad (44)$$

Multiplying from the left by G_c and from the right by G_c' , we find

$$G_{c\sigma}' = G_{c\sigma} + (G_{c\sigma} - 1) (e^{\mathcal{V}'_{\sigma} - \mathcal{V}_{\sigma}} - 1) G_{c\sigma}' \quad (45)$$

or

$$G_{\sigma} G_{c\sigma}'^{-1} = 1 + (1 - G_{c\sigma}) (e^{\mathcal{V}'_{\sigma} - \mathcal{V}_{\sigma}} - 1). \quad (46)$$

B. The QMC algorithm

We will now proceed to derive the Monte Carlo algorithm. The QMC algorithm involves changes in the Hubbard-Stratonovich field configuration $\{s_{\mathbf{i},l}\} \rightarrow \{s'_{\mathbf{i},l}\}$, and accepts these changes with the transition

probability $P_{s \rightarrow s'}$. Thus, to define the algorithm, we need $P_{s \rightarrow s'}$ and a relation between the cluster Green functions G and G' for the two different auxiliary field configurations. To simplify the notation, we introduce a combined space-time index $i = (\mathbf{i}, l)$, and will consider only local changes in the fields $s_m \rightarrow s'_m = -s_m$. As can be inferred from Eq. 40, the probability of a configuration $\{s_i\}$ is $P_s \propto \det(G_{c\uparrow\{s_i\}}^{-1}) \det(G_{c\downarrow\{s_i\}}^{-1})$; on the other hand detailed balance requires $P_{s'} P_{s' \rightarrow s} = P_s P_{s \rightarrow s'}$ for all s' . We may satisfy this requirement either by defining the transition probability $P_{s' \rightarrow s} = R/(1 + R)$, where

$$R \equiv \frac{P_s}{P_{s'}} = \frac{\det(G_{c\uparrow}') \det(G_{c\downarrow}')}{\det(G_{c\uparrow}) \det(G_{c\downarrow})} \quad (47)$$

is the relative weight of two configurations, or by letting $P_{s' \rightarrow s} = \text{minimum}(R, 1)$ (the first choice is called the ‘‘heat bath’’ algorithm, and the second the ‘‘Metropolis’’ algorithm). If the difference between two configuration is due to a flip of a single Hubbard Stratonovich field at the m th location in the cluster space-time [10], then from Eq. 46

$$R = \prod_{\sigma} [1 + (1 - G_{c\sigma m, m})(e^{-\alpha\sigma(s_m - s'_m)} - 1)]^{-1}. \quad (48)$$

For either the Metropolis or the heat bath algorithm, if the change is accepted, then we must update the Green function accordingly. The relationship between G and G' is defined by Eq. 45

$$G_{c'\sigma ij} = G_{c\sigma ij} + \frac{(G_{c\sigma im} - \delta_{i,m})(e^{-\alpha\sigma(s_m - s'_m)} - 1)}{1 + (1 - G_{c\sigma m, m})(e^{-\alpha\sigma(s_m - s'_m)} - 1)} G_{c\sigma mj}. \quad (49)$$

The QMC procedure is initialized by setting $G_{c\sigma ij} = \mathcal{G}_{ij}$ where \mathcal{G}_{ij} is the (cluster) Fourier transform of $\mathcal{G}(\mathbf{K})$ (Eq. 10), and choosing the corresponding field configuration with all $s_i = 0$. Then we use Eq. 49 to create a Green function corresponding to a meaningful field configuration (i.e. $s_i = \pm 1$, for each $i = (\mathbf{i}, l)$ or the $\{s_i\}$ from a previous run or iteration). We proceed by sequentially stepping through the space-time of the cluster, proposing local changes $s_i \rightarrow -s_i$. We accept the change if $P_{s' \rightarrow s}$ is greater than a random number between zero and one and update the Green function according to Eq. (49). After twenty to one hundred warm-up sweeps through the space-time lattice of the cluster, the system generally comes into equilibrium and we begin to make measurements. A few lattice updates are used between each measurement step to reduce the correlations between measurements. This improves the efficiency of the algorithm, since as we will see below, the measurements are numerically expensive. After many iterations of lattice updates, numerical round-off error begins to accumulate in the Green function update, Eq. 49. To compensate for this round-off error, the Green functions must be refreshed by again setting $G_{c\sigma ij} = \mathcal{G}_{ij}$, and then using Eq. 49 to recalculate the Green function corresponding to the present field configuration.

C. Differences with the BSS Algorithm

The Hirsch-Fye (HF) algorithm differs in several ways from the more familiar Blanckenbecker-Sugar-Scalapino (BSS) algorithm [26] used to simulate finite-sized systems.

The BSS algorithm is more efficient. HF simulations can be computationally quite expensive since the memory and the CPU time required by this algorithm scale as $(N_c N_l)^2$ and $(N_c N_l)^3$, where N_c and N_l are respectively the number of cluster sites and the number of time slices. The BSS algorithm scales as $N_l N_c^2$ for the memory and $N_l N_c^3$ for the CPU time. In order to study a meaningful set of cluster sizes using the Hirsch-Fye algorithm, it is necessary to use massively parallel computers. The maximum size we studied is $N_c = 64$ for the two-dimensional Hubbard model. This maximum size is indeed smaller than what can be reached with the BSS algorithm applied for finite system simulations (FSS). But, one should bear in mind that, in the DCA, the system is in the thermodynamic limit, it is the range of spatial correlations which is restricted to the cluster size. Cluster size effects are of different nature than that occurring in FSS. Therefore, the DCA as discussed in previous studies, can provide information which cannot be obtained from the FSS.

The Hirsch-Fye algorithm is action-based, whereas the BSS algorithm is Hamiltonian based. Therefore, the BSS algorithm cannot be employed to solve the DCA cluster problem, since the cluster problem has no Hamiltonian formulation with known parameters, and its action is highly non-local in time. The BSS algorithm requires that the action be local in time. The cluster action, Eq. 39, is long-ranged in time due to the term involving \mathcal{G} . Thus, the Hirsch-Fye algorithm is the most appropriate QMC algorithm to solve the DCA embedded cluster problem.

In addition to the differences mentioned above (detailed knowledge of the Hamiltonian is not needed for the HF algorithm so long as we have an initial Green function), there are other advantages to the HF algorithm. Whereas in the BSS algorithm, all degrees of freedom must appear explicitly, in the HF algorithm, any non-interacting degrees of freedom may be integrated out without loss of any information. At the end of the calculation, the irreducible diagrams on the interacting orbitals may be used to calculate any relevant quantity. Therefore, the HF algorithm may be used, for example, to simulate the periodic Anderson model (with only the f-orbital correlated) with the same computational cost required to simulate a single-band model. One may also incorporate a (dynamical) mean field coupling to an environment, or between an infinite set of coupled Hubbard planes [29], at no additional computational cost. In these cases, the information about the mean field coupling to the environment or the other planes is reflected in \mathcal{G} .

For clusters, the Hirsch-Fye algorithm is very stable at

low temperatures. In particular, the matrices G_c^σ which are generated in the algorithm are well-conditioned, the costly stabilization steps required at low temperatures [30,31] for the more popular BSS algorithm are avoided.

Finally, the Hirsch-Fye algorithm is easily adapted to making measurements which are non-local in time, such as those required to calculate the irreducible vertex functions. This will be discussed in the next section. It is very difficult to measure quantities which are non-local in time with the BSS algorithm. In fact, such measurements require significantly more CPU time than is required to average over the HHS field configurations, since the CPU time required by these measurements scales like $(N_c N_l)^3$ for both the BSS and Hirsch-Fye algorithms. Thus, when these measurements which are non-local in time are required, both algorithms scale like $(N_c N_l)^3$.

D. Making and Conditioning Measurements

In the QMC technique, all the physical quantities are expressed in terms of Green functions. Standard diagrammatic techniques are applied to evaluate these quantities. In doing so one must remember that the Hubbard-Stratonovich transformation reduces the problem to one of free electrons moving in a time-dependent field. Thus for each field configuration, any diagram may be formed by summing all allowed Wick's contractions. The full quantity is recovered by averaging this over all field configurations. Connected as well as disconnected configurations must be used during the evaluation. It is important to average over all equivalent time and space differences and all the symmetries of the Hamiltonian in order to produce the lowest variance measurement.

One difficulty encountered with the DCA algorithm is that a reliable transform from imaginary-time quantities, in the QMC part, to Matsubara frequencies, for the coarse-graining part is needed. A careful treatment of the frequency summation or the imaginary-time integration is crucial in order to ensure the accuracy and the stability of the algorithm and to maintain the correct high-frequency behavior of the Green functions. We need to evaluate the following integral

$$G_c(\mathbf{K}, i\omega_n) = \int_0^\beta d\tau e^{i\omega_n \tau} G_c(\mathbf{K}, \tau) \quad . \quad (50)$$

But from the QMC, we know the function $G_c(\mathbf{K}, \tau)$ only at a discrete subset of the interval $[0, \beta]$. As it may be readily seen by discretizing the above equation, the estimation of $G_c(\mathbf{K}, i\omega_n)$ becomes inaccurate at high-frequencies. This is formalized by Nyquist's theorem which tells us that above the frequency $\omega_c = \frac{\pi}{\Delta\tau}$ unpredictable results are produced by conventional quadrature techniques. For example, a rectangular approximation to the integral in Eq. 50 yields a $G(\mathbf{K}, i\omega_n)$ that is periodic in ω_n . This presents a difficulty since the causality requires that

$$\lim_{\omega_n \rightarrow \infty} G(\mathbf{K}, i\omega_n) \approx \frac{1}{i\omega_n} \quad . \quad (51)$$

A straightforward way to cure this problem may be to increase the size of the set of τ -points where the Green function is evaluated. But, this renders the QMC simulation rapidly intractable as seen in the previous section. A more economic way to avoid the problem is to use the high frequency information provided by an approximate method that is asymptotically exact.

Second-order perturbation theory is enough to obtain the correct asymptotic behavior, Eq. 51. To use this high frequency information, we compute the Matsubara-frequency Green function from the imaginary-time QMC Green function as follows [32]

$$G_c(\mathbf{K}, i\omega_n) = G_{cpt}(\mathbf{K}, i\omega_n) + \int_0^\beta d\tau e^{i\omega_n \tau} (G_c(\mathbf{K}, \tau) - G_{cpt}(\mathbf{K}, \tau)) \quad . \quad (52)$$

The integral is computed by first splining the difference $G_c(\mathbf{K}, \tau) - G_{cpt}(\mathbf{K}, \tau)$ using an Akima spline [33], and then integrating the spline (a technique often called oversampling).

As another example, consider the local magnetic susceptibility (used to calculate the screened local moment)

$$\begin{aligned} \chi(T) &\approx \frac{1}{N_c} \sum_{\mathbf{i}} \int_0^\beta d\tau \langle S_{\mathbf{i}}^+(\tau) S_{\mathbf{i}}^-(0) \rangle \\ &\approx \frac{1}{N_c} \sum_{\mathbf{i}} \int_0^\beta d\tau \langle c_{\uparrow\mathbf{i}}^\dagger(\tau) c_{\downarrow\mathbf{i}}(\tau) c_{\downarrow\mathbf{i}}^\dagger(0) c_{\uparrow\mathbf{i}}(0) \rangle \\ &\approx \frac{T}{2N_c} \sum_{\sigma\mathbf{i}} \int_0^\beta d\tau \int_0^\beta d\tau' \langle G_{c\sigma}(\mathbf{i}, \tau + \tau'; \mathbf{i}, \tau') \\ &\quad \times G_{c-\sigma}(\mathbf{i}, \tau'; \mathbf{i}, \tau + \tau') \rangle_{\{s_{i\ell}\}} \end{aligned} \quad (53)$$

where the $\{s_{i\ell}\}$ subscript indicates that the Monte Carlo average over the Hirsch-Hubbard-Stratonovich fields is still to be performed, and in the last step in Eq. 53 we form all allowed Wick's contractions and average over all equivalent time and spatial differences to reduce the variance of this estimator. This measurement is best accomplished by splitting it in two parts. First, we measure $\chi(\tau)$

$$\begin{aligned} \chi(\tau) &= \frac{T}{2N_c} \sum_{\sigma\mathbf{i}} \int_0^\beta d\tau' \langle G_{c\sigma}(\mathbf{i}, \tau + \tau'; \mathbf{i}, \tau') \\ &\quad \times G_{c-\sigma}(\mathbf{i}, \tau'; \mathbf{i}, \tau + \tau') \rangle_{\{s_{i\ell}\}} \end{aligned} \quad (54)$$

by approximating the integral as a sum using a rectangular approximation. For $\tau > 0$

$$\begin{aligned} \chi(\tau) &\approx \frac{1}{2N_l N_c} \sum_{\sigma\mathbf{i}\mathbf{l}'} \langle G_{c\sigma}(\mathbf{i}, \text{ind}(l+l'); \mathbf{i}, l') \\ &\quad \times G_{c-\sigma}(\mathbf{i}, l'; \mathbf{i}, \text{ind}(l+l')) \rangle_{\{s_{i\ell}\}} \end{aligned} \quad (55)$$

where $\text{ind}(l)$ is the smaller nonnegative value of either l or $l - N_l$. For $\tau = 0$ the fact that we always store $G_\sigma(\mathbf{i}, l'; \mathbf{i}, l') = G_\sigma(\mathbf{i}, \tau_l + 0^+; \mathbf{i}, \tau_l)$ requires us to modify the measurement

$$\chi(\tau = 0) \approx \frac{1}{2N_l N_c} \sum_{\sigma, l', \mathbf{i}} \langle G_{c\sigma}(\mathbf{i}, l'; \mathbf{i}, l') (G_{c-\sigma}(\mathbf{i}, l'; \mathbf{i}, l') - 1) \rangle_{\{s_i\}}. \quad (56)$$

Finally

$$\chi(T) = \int_0^\beta d\tau \chi(\tau) \approx \sum_l f(l) \Delta\tau \chi(\tau_l), \quad (57)$$

where the Simpson factor $f(l) = 2\Delta\tau/3$ ($4\Delta\tau/3$) for odd (even) l is used to reduce the systematic error of the integral.

As a final example, consider the cluster particle-particle Green function matrix $\chi_c(q, K, K')$ ($K = (\mathbf{K}, i\omega_n)$) which is used in Sec. III E 2 to calculate the lattice pair-field susceptibilities. The first step is to form the corresponding quantity in the cluster space-time

$$\chi_c(X_1, X_2, X_3, X_4) = \left\langle T_\tau c_\uparrow(X_1) c_\downarrow(X_2) c_\downarrow^\dagger(X_3) c_\uparrow^\dagger(X_4) \right\rangle. \quad (58)$$

Here X_i is in the space-(imaginary)time notation $X_i = (\mathbf{X}_i, \tau_i)$, where the points \mathbf{X}_i are on the corresponding reciprocal cluster of \mathbf{K} in real space, and $\langle T_\tau \dots \rangle$ denotes the time ordered averaging process. The two-particle Green functions are difficult to measure efficiently. For a particular configuration of the auxiliary Hubbard-Stratonovich fields, the fermions are noninteracting, thus the expectation value indicated above may be evaluated in two steps. First, using Wick's theorem, its value is tabulated for each field configuration $\{s_i\}$ and then transformed into the cluster Fourier space. Second, we Monte Carlo average over these configurations. After the first step, the expression for the above two-particle Green function in the cluster momentum-frequency space becomes

$$\begin{aligned} \chi_c(\mathbf{Q}, i\nu_n; \mathbf{K}, i\omega_n; \mathbf{K}', i\omega_{n'}) = & \left\langle \sum_{X_1, X_4} e^{iK'X_1} G_{c\uparrow}(X_1, X_4) e^{-iKX_4} \right. \\ & \left. \sum_{X_2, X_3} e^{i(Q-K')X_2} G_{c\downarrow}(X_2, X_3) e^{-i(Q-K)X_3} \right\rangle_{\{s_i\}}. \quad (59) \end{aligned}$$

where K is the momentum-frequency point $K = (\mathbf{K}, i\omega_n)$. The average over Hubbard-Stratonovich fields $\langle \dots \rangle_{\{s_i\}}$ can be evaluated through the QMC sweeps along with the measurements of $G_{c\uparrow}$ and $G_{c\downarrow}$. However, the sums (integrals) over τ in Eq. 59 require special consideration. Since the Green functions change discontinuously when the two time arguments intersect, the best applicable integral approximation is the trapezoidal approximation. Using this, we will run into Green functions $G_c(\mathbf{X}, \tau; \mathbf{X}, \tau)$ with both time and space arguments

the same. In the QMC algorithm, this is stored as $G_c(\mathbf{X}, \tau^+; \mathbf{X}, \tau)$ (i.e. it is assumed that the first time argument is slightly greater than the second); however, if we replaced the equal time Green function to be the average $\{G_c(\mathbf{X}, \tau^+; \mathbf{X}, \tau) + G_c(\mathbf{X}, \tau; \mathbf{X}, \tau^+)\}/2 = G_c(\mathbf{X}, \tau^+; \mathbf{X}, \tau) - 1/2$ then a trapezoidal approximation of the integrals results. If we call the matrix \mathbf{G}_c , with $1/2$ subtracted from its diagonal elements, as $\hat{\mathbf{G}}_c$ (note that we can treat one of the three independent momenta involved in χ_c as a variable Q outside the matrix structure), then we can write the two-particle Green function in a matrix form

$$\chi_{c_{ij}}(\mathbf{Q}) = \left\langle \left(\mathbf{F}_{\mathbf{Q}=0}^\dagger \hat{\mathbf{G}}_{c\uparrow} \mathbf{F}_{\mathbf{Q}=0} \right)_{ij} \left(\mathbf{F}_{\mathbf{Q}}^\dagger \hat{\mathbf{G}}_{c\downarrow} \mathbf{F}_{\mathbf{Q}} \right)_{ij}^* \right\rangle_{\{s_i\}}, \quad (60)$$

where $(\mathbf{F}_{\mathbf{Q}})_{ij} = \Delta\tau e^{-i(\mathbf{K}_j - \mathbf{Q}) \cdot \mathbf{X}_i - i\omega_j \tau_i}$ where we have chosen i and j to index the cluster momentum-frequency space. This measurement may be performed efficiently if the product of three matrices in each set of parenthesis is tabulated as two sequential matrix-matrix products and stored before the direct product between the terms in parenthesis is calculated. When done this way, the calculation time required for this process scales like $(N_c N_l)^3$ rather than $(N_c N_l)^4$ as would result from a straightforward evaluation of the sums implicit in Eq. 60.

For the reasons discussed above, Eq. 60 becomes unreliable at high frequencies $|\omega_n| > \pi/\Delta\tau$. The high frequency behavior of the two particle Green function can be recovered by using a method similar to that developed for the one particle Green function [34]. The first term of its perturbation expansion, the bubble diagram, is used for the conditioning. It is calculated in two ways: First it is formed from the square of the properly conditioned cluster Green function. Second, it is calculated using the same approximation to the Fourier transform employed in Eq. 60. The difference of the two may be used to condition the estimate

$$\begin{aligned} \chi_{c_{ij}}(\mathbf{Q}) = & \left\langle \left(\mathbf{F}_{\mathbf{Q}=0}^\dagger \hat{\mathbf{G}}_{c\uparrow} \mathbf{F}_{\mathbf{Q}=0} \right)_{ij} \left(\mathbf{F}_{\mathbf{Q}}^\dagger \hat{\mathbf{G}}_{c\downarrow} \mathbf{F}_{\mathbf{Q}} \right)_{ij}^* \right\rangle_{\{s_i\}} - \\ & \left(\mathbf{F}_{\mathbf{Q}=0}^\dagger \left\langle \hat{\mathbf{G}}_{c\uparrow} \right\rangle_{\{s_i\}} \mathbf{F}_{\mathbf{Q}=0} \right)_{ij} \left(\mathbf{F}_{\mathbf{Q}}^\dagger \left\langle \hat{\mathbf{G}}_{c\downarrow} \right\rangle_{\{s_i\}} \mathbf{F}_{\mathbf{Q}} \right)_{ij}^* \\ & + G_c(K_i) G_c^*(K_i - Q) \delta_{ij}. \quad (61) \end{aligned}$$

Moreover, this appends the right asymptotic behavior of the perturbation result to the two-particle Green function at high frequencies where QMC results are dominated by statistical errors.

E. Optimizing the Code

In this subsection, we will discuss the optimization and parallelization of the QMC code.

We generally find that the heat bath algorithm is more efficient, presumably because it has a lower acceptance rate and therefore deemphasizes the expensive step of updating the Green function.

We may greatly reduce the statistical error in many of the measured Green functions by employing the translational and point-group symmetries of the cluster. The QMC averaging over the HHS fields systematically restores the translational invariance of the system in time and space. So we may reduce the statistical error in the measured Green functions by averaging over all equivalent differences in spatial and temporal cluster coordinates. To reduce the statistical error further, we then average over all the lattice point group operations. For example, for $G_c(\mathbf{K}, \omega_n)$

$$G_c(\mathbf{K}, i\omega_n) = \frac{1}{N_{\mathcal{R}}} \sum_{\mathcal{R}} G_c(\mathcal{R}(\mathbf{K}), i\omega_n) \quad (62)$$

where \mathcal{R} is one of the symmetry operations in the point group of the lattice and $N_{\mathcal{R}}$ is the total number of such symmetry operations.

The two-particle Green functions typically have more statistical noise than their single-particle counterparts, and their matrices can be quite large. To reduce both the storage needed for these measurements and their statistical noise, the point group symmetry of the lattice may again be used. We first average the two-particle cluster Green functions over the different point-group operations

$$\chi_{\sigma, \sigma'}(q, \mathbf{K}, \mathbf{K}') = \frac{1}{N_{\mathcal{R}}} \sum_{\mathcal{R}} \chi_{\sigma, \sigma'}(q, \mathcal{R}(\mathbf{K}), \mathcal{R}(\mathbf{K}')) \quad (63)$$

We should also average over the symmetries of the diagrams. I.e., for the particle-particle channel there are additional symmetries of the diagrams which include horizontal $(\mathbf{K}, i\omega_n; \mathbf{K}', i\omega_{n'}) \rightarrow (\mathbf{K}', i\omega_{n'}; \mathbf{K}, i\omega_n)$ and vertical $(\mathbf{K}, i\omega_n; \mathbf{K}', i\omega_{n'}) \rightarrow (-\mathbf{K}, -i\omega_n; -\mathbf{K}', -i\omega_{n'})$ reflections. After these symmetries have been imposed, we will lose no information and significantly reduce the storage requirements if we store $\chi_{\sigma, \sigma'}(q, \mathbf{K}, \mathbf{K}')$ for either \mathbf{K} or \mathbf{K}' within the irreducible wedge (we may not take both \mathbf{K} and \mathbf{K}' within the irreducible wedge though).

The memory required for these calculations may be further minimized by limiting the use of the double precision arithmetic. The Green functions and all of the equations associated with the calculation of the initial Green function and the Green function update, Eq. 49, are computed with double precision (8 byte real) to minimize the problems with the accumulation of numerical error discussed in Sec. IV B. However, to save memory, it is convenient to both calculate and store the two-particle cluster Green functions with single precision (8 byte complex). Since these measurements typically have a fraction of a

percent statistical error, higher precision arithmetic and storage will not improve the accuracy of the two-particle measurements.

The required CPU time may be reduced by optimizing the inner loops. The two numerically most expensive parts of the QMC code are the Green function update, Eq. 49, and the two-particle measurements, Eq. 61. These can be written in terms of highly-optimized BLAS calls [35], DGER and CGEMM, respectively. To see that Eq. 49 can be calculated with an outer product, we define

$$a_m = \frac{(e^{-\alpha\sigma(s_m - s'_m)} - 1)}{1 + (1 - G_{c\sigma m, m})(e^{-\alpha\sigma(s_m - s'_m)} - 1)} \quad (64)$$

Then Eq. 49 takes the form

$$G_{c' \sigma ij} = G_{c\sigma ij} + (G_{c\sigma im} - \delta_{i, m})a_m G_{c\sigma mj} \quad (65)$$

This is a vector outer product and matrix update, with vectors $a_m(G_{c\sigma im} - \delta_{i, m})$ and $G_{c\sigma mj}$ for fixed m .

Additional speedup of the calculation is possible by writing parallel codes. The DCA-QMC codes are extremely well suited for massively parallel supercomputers because of their efficient use of the floating-point capabilities of such machines and the highly parallel nature of the codes and the underlying algorithm. With the current relative decline in the availability of vector supercomputers and the concomitant increase in the number of massively parallel supercomputers, this is an important feature of the algorithm. In the remainder of this subsection, we discuss first the general parallel nature of the algorithm.

There is a high degree of parallelism in the DCA-QMC algorithm, which one may exploit. This parallelism exists on two levels. First, QMC is itself inherently parallel because it consists of a number of stochastic random-walks. One may think of QMC as one long Markov-chain walk. Measurements are made periodically along this walk. At the end of the walk, these measurements are averaged and the final result, with error bars, is obtained.

However, there is no reason why this Markov-chain walk has to be continuous. It has been known for years that one can perform several independent, shorter Markov-chain walks and average the results of each walk to obtain the final result of the calculation. The result can be an almost perfect parallel speedup as an increasing number of processors is applied to a problem. This arises because only an extremely small amount of communication between processors is required – first to initialize the Markov-chain walks and then to collect the data for averaging at the end of the Markov process (even this averaging can be done in parallel using MPI calls). We call this the “Perfectly Parallel” algorithm.

The second degree of parallelism exists in the linear algebra problem itself. That is, one can distribute the vectors and matrices which comprise the linear algebra problem across several processors. (The matrix in our case is the Green function discussed above.) Such a break-up

of the data becomes of paramount importance when the size of a matrix is so large that it cannot possibly fit within all of the memory available on a single processor of a computer.

The issue of interprocessor communication now becomes paramount as one performs linear algebra. However, two things work in our favor here. First, the main linear algebra operation of the QMC is a vector outer product – which is in itself inherently parallel. Second, this is a well-studied problem and again an efficient library package, the parallel PBLAS [35], exists to solve it. When we divide the Green function over all of the processors that we use in a run on a parallel machine, we call this the “Truly Parallel” method.

The Truly Parallel method can be used to efficiently fill all available processors of a parallel machine with one DCA–QMC problem. Often, however, the problem of interest is not so big as to require the entire machine for one Green function, but is too big to fit within the RAM available on a single processor and hence too big for the Perfectly Parallel code. To efficiently use available hardware for these problems, one can employ a “Hybrid” code, which is both truly parallel in part and perfectly parallel in part.

The hybrid code may be thought of as using blocks of processors to distribute Green functions and in turn performing a perfectly parallel QMC with many such blocks. For example, say that the Green function for the problem at hand will not fit in the memory of a single processor, but will fit within the memory of 4 processors. Assume also that there are 100 processors available for a run. The hybrid code then allocates all 100 processors, divides these 100 processors into 25 blocks of 4, distributes copies of the initial Green function onto each of the 25 blocks, and then does a perfectly parallel QMC using these 25 blocks. This makes the most use of the resources of a machine and is especially well-suited for a Symmetric Multi-Processor machine, where many nodes exist and each node comprises several processors with a shared, relatively large, pool of RAM.

V. THE DCA ALGORITHM

In this section, we will discuss how the QMC and DCA formalism are combined into a DCA algorithm for simulating lattice problems. The complete DCA program is made of three completely separate parts as illustrated in Fig. 7. The first part is the self-consistent loop which is the main part of the algorithm. It includes the DCA self-consistency loop composed of the QMC block and the coarse-graining of the lattice. This program is usually run on a parallel supercomputer, and the cluster self energy and the various two-particle cluster Green functions are written into files. In the second part various one-particle and two-particle lattice Green functions are calculated from the cluster Green functions obtained from

the self-consistent loop. This part of the code is generally run on a workstation and it requires in the data generated by the first part of the code. The third is devoted to the analytical continuation of the imaginary-time Green functions to real frequencies using the Maximum Entropy Method (MEM).

A. Part 1: The self-consistent loop

1. The DCA iteration procedure is started by setting the initial self-energy $\Sigma_c(\mathbf{K}, i\omega_n) = 0$, or to a perturbation theory result.
2. Σ is then used to compute the coarse-grained Green function $\bar{G}(\mathbf{K}, i\omega_n)$,

$$\bar{G}(\mathbf{K}, i\omega_n) = \sum_{\bar{\mathbf{k}}} \frac{1}{i\omega_n - \epsilon - \epsilon_{\mathbf{K}+\bar{\mathbf{k}}} - \Sigma_c(\mathbf{K}, i\omega_n)}. \quad (66)$$

3. The next step of the iteration is to use $\bar{G}(\mathbf{K}, i\omega_n)$ to compute the host Green function $\mathcal{G}(\mathbf{K}, i\omega_n)^{-1} = \bar{G}(\mathbf{K}, i\omega_n)^{-1} + \Sigma_c(\mathbf{K}, i\omega_n)$ which must be introduced to avoid over-counting diagrams. $\mathcal{G}(\mathbf{K}, i\omega_n)$ serves as the input to the QMC simulation to yield a new estimate for the cluster self-energy.
4. $\mathcal{G}(\mathbf{K}, i\omega_n)$ must be Fourier transformed from the momentum-frequency variables to space-imaginary-time variables before being introduced in the QMC part of the program as the initial Green function $G_{cij} = \mathcal{G}(\mathbf{X}_i - \mathbf{X}_j, \tau_i - \tau_j)$ corresponding to all $s_i = 0$. Eq. 49 is used to generate the cluster Green function corresponding to $s_i = 1$, or to the $\{s_i\}$ from a previous run.
5. The QMC step is next and is the most time consuming part of the algorithm. Each QMC step is warmed up before one starts to perform measurements. While making measurement, we average over the differences in space and time and the point group operations, as described above, to reduce the statistical error. This together with the QMC averaging restores the translational invariance of the system in time and space, so $\langle G_{cij} \rangle_{\{s_i\}} = G_c(\mathbf{X}_i - \mathbf{X}_j, \tau_i - \tau_j)$.
6. $G_c(\mathbf{X}_i - \mathbf{X}_j, \tau_i - \tau_j)$ is then Fourier-transformed to $G_c(\mathbf{K}, i\omega_n)$. We calculate a new estimate for the self-energy $\Sigma_c(\mathbf{K}, i\omega_n) = \mathcal{G}(\mathbf{K}, i\omega_n)^{-1} - G_c(\mathbf{K}, i\omega_n)^{-1}$.
7. Starting with step 2, the procedure is repeated until $\Sigma_c(\mathbf{K}, i\omega_n)$ converges. This typically happens in less than ten iterations. The number of iterations decreases when N_c increases since the coupling to the host is smaller ($\mathcal{O}(1/N_c)$) [9] for larger clusters.

The convergence test is made on the ratio ρ ,

$$\rho = \frac{|\sum_{\mathbf{K}}(\Sigma_{cnew}(\mathbf{K}, i\omega_0) - \Sigma_{cold}(\mathbf{K}, i\omega_0))|}{|\sum_{\mathbf{K}} \Sigma_{cold}(\mathbf{K}, i\omega_0)|} \quad (67)$$

where $\omega_0 = \pi T$

8. Once convergence is reached to the desired accuracy, the remaining one and two-particle measurements are made in a final QMC iteration. As in a usual QMC simulation, bins of measurements are accumulated and error estimates are made from the fluctuations of the binned measurements. These error estimates are accurate provided that the bins contain enough measurements so that the bin-averages are uncorrelated. The statistical error may be reduced by averaging over the different symmetries as discussed above.

Once the cluster Green functions are obtained, the determination of the lattice quantities requires additional steps which are done in separate programs.

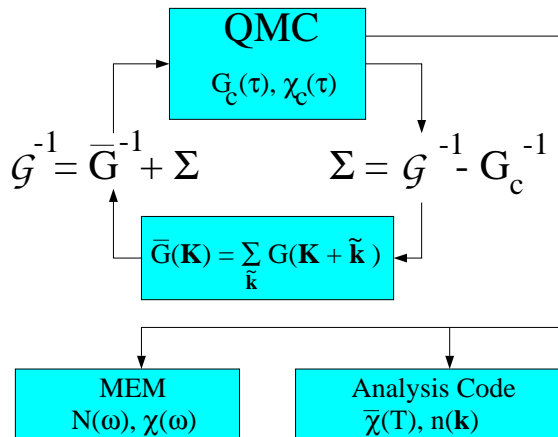


FIG. 7. Sketch of the DCA algorithm: the self-consistent loop, the analysis part and the MEM part.

B. Part 2: Numerical calculation of lattice quantities

The self-consistent loop yields cluster Green functions $G_c(\mathbf{K}, i\omega_n)$, $\Sigma_c(\mathbf{K}, i\omega_n)$, and susceptibilities $\chi_{c\sigma,\sigma'}(\mathbf{K}, i\omega_n; \mathbf{K}', i\omega_m)$, $\Pi_g(\mathbf{K}, i\omega_n; \mathbf{K}', i\omega_m)$ which may be used to construct the equivalent lattice quantities. This is done in a separate computer program in which the irreducible quantities of the cluster which are in the DCA approximation identical to those of the lattice are used to compute the corresponding reducible lattice quantities.

To calculate the single-particle quantities, an interpolated self-energy $\Sigma(\mathbf{k}, i\omega_n)$ may be used. This is especially important for the calculation of $|\nabla n(\mathbf{k})|$, and other quantities such as band structure, where continuity of the self energy is important. We often use bilinear interpolation for this purpose, since it is guaranteed to preserve the sign of function (i.e. the bilinear interpolation of a

positive-definite function remains everywhere positive). We also use a multidimensional spline interpolant, like some Akima splines, which does not overshoot. However, it is important to note that this interpolated self-energy should not be used in the self-consistent loop as this can lead to violation of causality [8].

The interpolated self energy, $\Sigma(\mathbf{k}, i\omega_n)$ is then used to calculate the Fermi surface. For this we use the discrete form of $\nabla n(\mathbf{k})$

$$\frac{\Delta n_{\mathbf{k}}}{\Delta \mathbf{k}} = \frac{T \sum_n G(\mathbf{k} + \Delta \mathbf{k}, i\omega_n) - G(\mathbf{k}, i\omega_n)}{\Delta \mathbf{k}} \quad (68)$$

which, in a Fermi liquid (or a marginal Fermi liquid) is maximum at the Fermi surface. The quasiparticle weight may be approximated with

$$Z_{\mathbf{k}} \approx 1 - \frac{Im \Sigma(\mathbf{k}, i\omega_{n=0})}{\omega_{n=0}} \quad (69)$$

which becomes exact as $T \rightarrow 0$.

The calculation of the lattice susceptibilities in the particle-hole channel and in the particle-particle channel is also made in this code. The stored QMC cluster susceptibilities are used for this purpose as prescribed in Sec. III E. Here, we first form the corresponding coarse-grained and bare cluster susceptibilities, and then we use Eq. 20 to calculate the corresponding coarse-grained lattice susceptibility. To calculate the pair field susceptibilities, we first calculate the corresponding coarse-grained two-particle reducible vertex, and then use Eq. 29 to calculate the coarse-grained lattice pair-field susceptibility matrix.

In the two-particle calculations, it is tempting to interpolate the cluster vertex functions to the lattice momenta. However, this would increase the size of the matrices which must be inverted in Eq. 20 dramatically, making the calculation of the lattice susceptibilities numerically much more expensive.

C. Part 3: Analytic continuation

Unfortunately, there is no reliable way to perform the direct analytic continuation of $\Sigma_c(\mathbf{K}, i\omega_n)$. Padé approximants lead to very unstable spectra because of the QMC statistical noise contained in $\Sigma_c(\mathbf{K}, i\omega_n)$. The binned imaginary-time Green function data accumulated from the cluster calculation must be used to obtain lattice spectra from which $\Sigma_c(\mathbf{K}, \omega)$ may be deduced. To obtain the self-energy and spectral-weight function $A(\mathbf{k}, \omega)$ of the lattice in real frequencies, we first compute the cluster spectral-weight $\bar{A}(\mathbf{K}, \omega)$. This is done using the Maximum entropy method [15] to invert the following integral equation

$$\bar{G}(\mathbf{K}, \tau) = \int d\omega \frac{e^{-\omega\tau}}{1 + e^{-\beta\omega}} \bar{A}(\mathbf{K}, \omega) \quad , \quad (70)$$

where $\bar{G}(\mathbf{K}, \tau)$ is the imaginary-time Green function obtained from the QMC simulation of the cluster.

Since $\bar{A}(\mathbf{K}, \omega) = -1/\pi \text{Im} \bar{G}(\mathbf{K}, \omega)$, the full frequency-dependent coarse-grained Green function $\bar{G}(\mathbf{K}, \omega)$ is obtained using Kramers-Kronig relations. Then, the equation

$$\bar{G}(\mathbf{K}, \omega) = \frac{N_c}{N} \sum_{\bar{\mathbf{k}}} \frac{1}{\omega - \epsilon - \epsilon_{\mathbf{K}+\bar{\mathbf{k}}} - \Sigma_c(\mathbf{K}, \omega)} \quad (71)$$

is solved for the real-frequency self-energy $\Sigma_c(\mathbf{K}, \omega)$ using a complex root finder [36]. This self energy may then be interpolated onto the lattice \mathbf{k} points using a high-level interpolant which also preserves the sign of the imaginary part.

The above steps are unnecessary if the local quantities are to be computed since the local lattice and cluster Green functions correspond one-to-one. For example, we may directly analytically continue the local cluster Green function to obtain the lattice density of states.

VI. APPLICATION TO THE 2D HUBBARD MODEL

We will now show the results of the application of the DCA to the two-dimensional Hubbard model. The Hubbard model has a long history and is believed to contain the mechanism of various physical phenomena such as magnetism, metal-insulator transitions and more recently superconductivity and non-Fermi liquid behavior. Our intent in this section is not to exhaustively study this model's properties, but rather to use it to illustrate the power and limitations of the DCA and to survey what can be done.

Since the two-dimensional model is not expected to have a finite-temperature magnetic or perhaps even superconducting transition, we will add a hopping t_{\perp} [37] into the third dimension between an infinite set of weakly coupled Hubbard planes

$$t_{\perp}(k_x, k_y, k_z) = -2t_{\perp}(\cos k_x - \cos k_y)^2 \cos k_z. \quad (72)$$

We take $t_{\perp} \ll t$, and treat the additional coupling at the DMFA level, so the self-energy is independent of k_z . This is accomplished by modifying the coarse-graining cells into rectangular solids of dimensions Δk , Δk and 2π in the k_x , k_y and k_z directions, respectively. After coarse-graining, the problem is reduced to a two-dimensional cluster. Information relevant to the mean-field coupling between the planes is contained within \mathcal{G} .

A. Results at Half-filling

The physics of the half filled model is a severe test of the DCA as well as finite-sized simulations (FSS) due to the quantum critical point at zero doping. As this point

is approached, both the dynamical and spatial correlation lengths diverge, and both the DCA and FSS are expected to fail.

1. Antiferromagnetism

Earlier finite size simulations [38,39] employing the QMC method have led to the conclusion that the ground state is an antiferromagnetic insulator at half-filling. Since the model is two dimensional, we know from the Mermin-Wagner theorem that the transition temperature is necessarily zero. But as found in infinite dimensions [32], the DMFA predicts a finite temperature transition even in two dimensions. This spurious behavior may be attributed to the lack of non-local correlations in the DMFA. These correlations are known to induce strong fluctuations particularly in reduced dimensions and are responsible for the suppression of the finite temperature transition. The DCA which includes these non-local correlations is thus expected to progressively drive the spurious finite temperature transition found in the DMFA towards zero temperature as the cluster size increases.

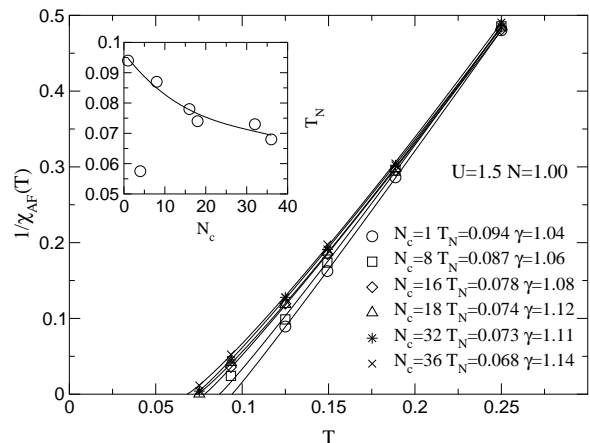


FIG. 8. The inverse antiferromagnetic susceptibility versus temperature for various cluster sizes. The lines are fits to the function $(T - T_N)^\gamma$. In the inset, the corresponding Neél temperatures, determined by the divergence of the susceptibility, are plotted. The line is a polynomial fit to the data, excluding $N_c = 4$.

This behavior is illustrated in Fig. 8, where the inverse antiferromagnetic susceptibility is plotted versus temperature for $\delta = 0$ and various values of N_c which preserve the lattice symmetries as discussed in Sec. III C. At high temperatures, the susceptibility is independent of N_c , due to the lack of non-local correlations. In contrast to FSS calculations, the low temperature susceptibility diverges at $T = T_N$, indicating an instability to an antiferromagnetic phase. As N_c increases $N_c > 1$, the non-local dynamical fluctuations included in the DCA suppress the antiferromagnetism. For example, when $N_c = 1$, the susceptibility diverges with an exponent

$\gamma \approx 1$, as expected for a mean-field theory; whereas the susceptibilities for larger N_c values diverge at lower temperatures with larger exponents indicative of fluctuation effects [41]. At first, these effects are pronounced; however, as N_c increases, T_N falls and γ rises more slowly with increasing N_c . This can be understood from the singular nature of the spin correlation length, which at least in the large U limit is expected to vary as $\xi \propto e^{A/T}$, where A is a constant of the order of the exchange coupling. For this quantum critical transition, we expect the DCA to indicate a finite temperature transition once ξ exceeds the linear cluster size. Since correlations build exponentially, large increases in the cluster size will only reduce the DCA transition temperature logarithmically.

Note that the data for $T_N(N_c)$ falls on a smooth curve, except for $T_N(N_c = 4)$. This behavior was seen previously in the transition temperature of the Falicov-Kimball model, calculated with DCA. [7,8] The $N_c = 4$ data falls well off the curve produced by the other data, and has a much larger exponent indicating that fluctuation effects are more pronounced. Presently this behavior is not completely understood but may be related to the fact that the maximum coordination number for $N_c = 4$ is two, whereas it is greater than two for cluster sizes larger than $N_c = 4$.

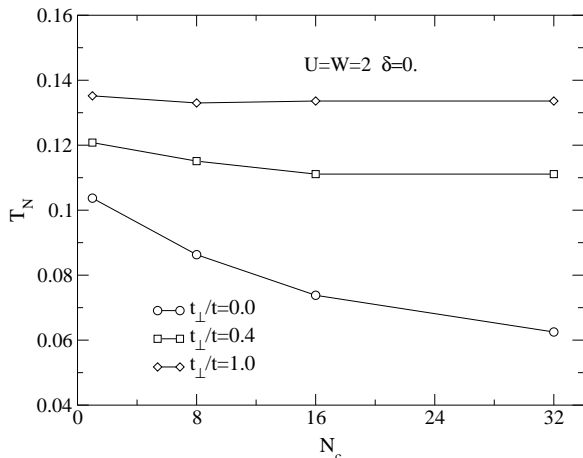


FIG. 9. T_N versus N_c for different values of t_\perp/t

An interplanar coupling can significantly alter the phase diagram. However, since the superexchange coupling varies roughly like the square of the hopping, it is necessary to make t_\perp a significant fraction of the intraplanar coupling t in order to see an effect. For example, if $t_\perp/t = 0.4$, the ratio of the interplanar to intraplanar exchanges is roughly $J_\perp/J \approx 0.16$. In Fig. 9 the antiferromagnetic transition temperature is plotted versus N_c when $t_\perp/t = 0, 0.4, 1.0$ when $U = W = 2$ and $\delta = 0$. For both $t_\perp/t = 0.4$ and $t_\perp/t = 1.0$, the transition temperatures for $N_c = 16$ and 32 are the same to within the numerical error. Thus, the finite-temperature transitions found for small clusters, can be preserved as $N_c \rightarrow \infty$ by introducing the interplanar coupling.

2. Mott transition at half-filling

In the strong coupling limit, a Mott Hubbard gap is expected to open in the charge excitation spectra. In the weak coupling limit, the situation is less clear. Since the ground state of the half filled model is always an antiferromagnet, the system remains insulating, but the nature of the insulating state in weak coupling is less clear, and depends upon the dimensionality. In one dimension, Lieb and Wu [40] showed long ago that a charge gap opens as soon as $U > 0$. There is a spin-charge separation and there is no long range order, even at $T = 0$. Hence, the Slater scenario is not responsible for the metal-insulator transition and the low energy spin excitations are described by the Heisenberg model. In infinite dimension, the model can be mapped to a self-consistent Anderson impurity problem. The solution of the self-consistent equations have been obtained numerically by various authors. For small $U \ll W$, the antiferromagnetic transition temperature T_N is higher than any temperature at which there is a metal-insulator transition in the paramagnetic phase. Hence, the metal-insulator transition in infinite dimension is due to the Slater mechanism. In two dimensions, the Mermin-Wagner theorem prohibits long range order for any $T > 0$, and we find that the weak coupling transition is similar to what is found in one dimension.

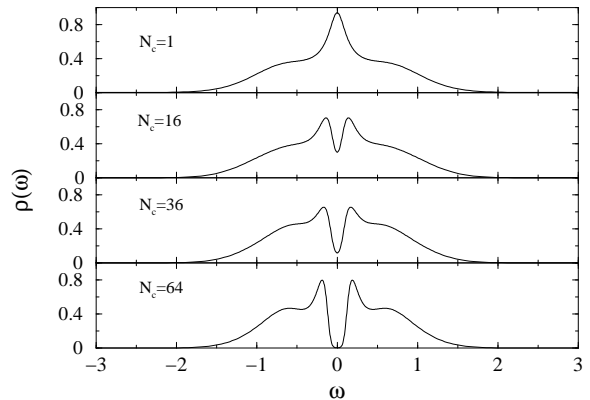


FIG. 10. The single-particle density of states $\rho(\omega)$ at $\beta = 32$, $U = 1$, and $t_\perp = 0$.

The density of states $\rho(\omega)$ (shown in Fig. 10) confirms the destruction of the Fermi liquid quasi-particle peak by short-range antiferromagnetic correlations. With increasing N_c , the gap opens fully, and the Hubbard side bands become more pronounced.

In Fig. 11 the behavior of T_N is compared to the temperature T_g where the gap opens. In contrast to T_N , T_g increases with the size of the cluster. This confirms the conclusion that a gap, which is not due to antiferromagnetism alone, opens at finite temperatures in the 2D Hubbard model.

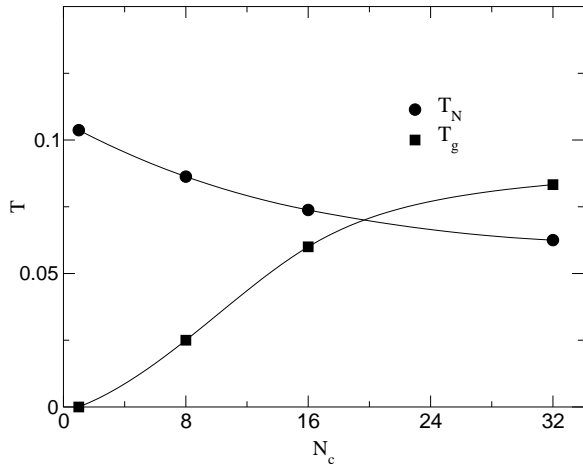


FIG. 11. The Neel, T_N , and gap, T_g , temperatures versus N_c when $U = W = 2$, $\delta = 0$ and $t_{\perp} = 0$.

3. Comparisons with finite system simulations

A great number of simulations have been performed in the half-filling regime of the two-dimensional Hubbard model over the last decade. Most of them are based on QMC with imaginary-time data analytically continued by the maximum entropy method. While these studies all agree for $U > W$, for $U < W$ they have led to conflicting results [16]. The reason is that the metal-insulator transition is related to the antiferromagnetic transition so that it is difficult to distinguish between the two physical processes. As a consequence various conflicting scenarios for the disappearance of the quasiparticle peak at low temperatures have been proposed. These controversies are inherent to the limitations of the finite system simulations. There are artificially introduced finite size gaps when the correlations become comparable to the system size. This does not occur when $U > W$ because the Mott gap opens well before the magnetic correlations set in. It is thus fair to ask to what extent the conclusion reached with the DCA above may be more reliable. For this it is necessary to compare the DCA to FSS.

In Fig. 12 and Fig. 13, we show the imaginary-time Green function $G(\tau)$ at the Fermi point $X = (\pi, 0)$. This quantity has a more rapid decay from its maximum at $G(\beta/2)$ when the effects of the correlations are stronger. In finite systems, the decay is sharper for smaller lattices while in the DCA it is the opposite. This behavior marks the fundamental difference between the FSS and the DCA. At low temperatures, in FSS, the correlation length is greater than the lattice size. Thus, the effects of the correlations are overestimated for smaller clusters because these systems are artificially closer to criticality than a system in the thermodynamic limit. This tendency is reduced by increasing the cluster size, which moves the system in the direction of the thermodynamic limit. The situation is radically different in the DCA where the system is already in the thermodynamic limit. The DCA approximation consist in restricting correla-

tions to within the cluster length in the infinite system. As the cluster size increases, possible longer-range correlations are progressively included. Thus, the effects of the correlations increase with the cluster size.

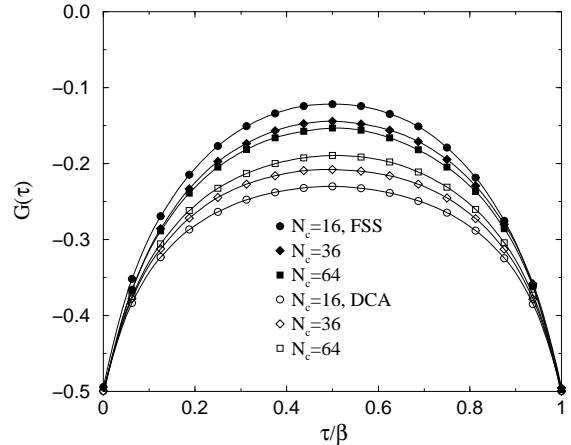


FIG. 12. The imaginary-time Green function at the point $X = (\pi, 0)$ on the Fermi surface from finite size QMC (filled symbols) and from DCA (open symbols) with $U = 1.1$, $\beta = 16$, $t_{\perp} = 0$ and $N_c = 16, 36, 64$. The size increases from top to bottom for FSS. The size increases from bottom to top for DCA.

The density of states shown in Fig. 13 supports these conclusions. The finite size gap in the FSS decreases when the cluster size goes from $N_c = 16$ to 64. While, in the DCA for $N_c = 16$ there is a pseudogap that turns into a true gap when the cluster size is increased to 64. Since by construction, the DCA underestimates the gap, we can affirm that at this temperature, the gap exists in the thermodynamic limit. Its actual value is bracketed by the FSS and the DCA. This behavior is characteristic of the DCA. It has been extensively verified on the one-dimensional Hubbard model [14].

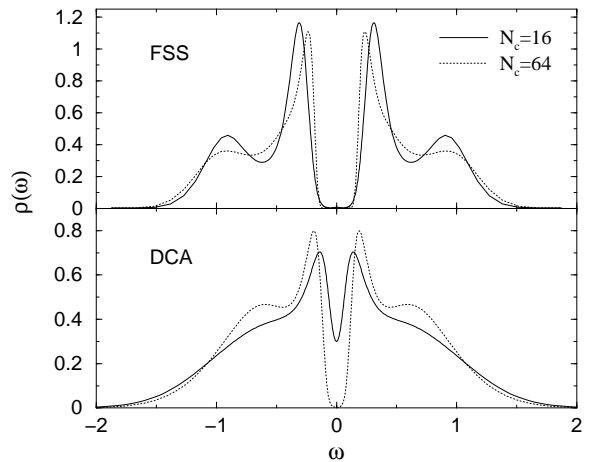


FIG. 13. The density of states $\rho(\omega)$ from finite size QMC (top) and from DCA (bottom) at $U = 1$, $\beta = 32$, $t_{\perp} = 0$ and $N_c = 16, 64$.

B. Results away from half-filling

1. Sign Problem

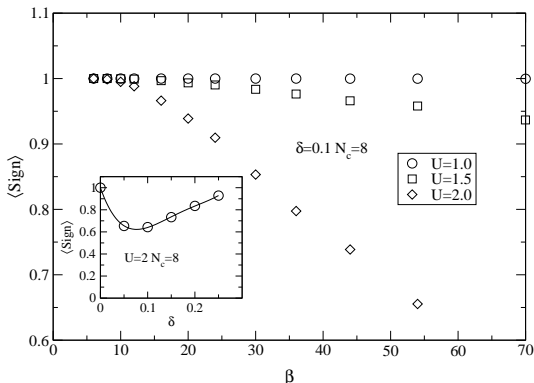


FIG. 14. The average sign as function of the inverse temperature β for $N_c = 8$ at $\delta = 0.1$ for $U = 1.0, 1.5, 2.0$. In the inset, the average sign is plotted versus doping δ when $U = W = 2$, $t_{\perp} = 0$ and $\beta = 54$.

The most serious limitation of QMC calculations at low temperatures is the sign problem. Off half-filling, the sign of $P(\{s_i\}) \propto \det[G_c^{\uparrow}(\{s_i\})] \times \det[G_c^{\downarrow}(\{s_i\})]$ can be negative so that it can no longer be interpreted as a probability distribution. The solution is to reinterpret $|P(\{s_i\})|$ as the probability of the configuration $\{s_i\}$ and associate its sign with the measurement. [42] For any operator O , this becomes

$$\langle O \rangle = \frac{\sum_{\{s_i\}} P(\{s_i\}) O(\{s_i\})}{\sum_{\{s_i\}} P(\{s_i\})} = \frac{\sum_{\{s_i\}} \text{sign}(\{s_i\}) O(\{s_i\})}{\sum_{\{s_i\}} \text{sign}(\{s_i\})} \quad (73)$$

where $\text{sign}(\{s_i\})$ is the sign of $P(\{s_i\})$, $O(\{s_i\})$ is the value of the operator for the field configuration $\{s_i\}$, and the primed sums are over configurations generated by importance sampling. In finite system simulations, as the temperature is lowered, the average sign becomes exponentially small [42,30] so that it is no longer possible to obtain good statistics. This sign problem has posed a formidable challenge in the field of numerical simulations for nearly two decades.

Some recent works have brought some hope. Gubernatis and Zhang [43] and Zhang [44] have shown that by putting a constraint on the fermion determinant, one can construct an approximate algorithm which shows some improvement on this problem. While the resulting algorithm seems to be free from the sign problem, it is possible that the constraint introduced may affect the ergodicity of the algorithm. The ergodicity question is suggested by the work of Sorella [45] who employ a similar idea as the former authors but who arrived at different results. The most promising new direction seems to be that of Chandrasekharan and Weise [46]. They proposed a new algorithm which is rigorously free from a sign problem for certain classes of models. The basic idea is to decompose

a configuration of fermion world-lines into clusters that contribute independently to the sign. There are two type of clusters: clusters whose flip changes the sign called meron and others that do not modify the sign after a flip. Configurations containing meron-clusters contribute 0 to the partition function, while all other configurations contribute 1. Hence, this cluster representation describes the partition function as a gas of clusters in the zero-meron sector.

The sign problem remains in DCA simulations, as illustrated in Fig. 14 where the average sign is plotted versus inverse temperature for various values of U when $\delta = 0.1$ and $N_c = 8$. In the inset, the average sign is plotted versus doping when $U = W = 2$, $\beta = 54$ and $N_c = 8$. As in FSS, the sign is worst just off half filling. However, the DCA sign problem is significantly less severe than that encountered in FSS. This is illustrated in Fig. 15 where the average sign for the DCA and the BSS simulations of White *et al.* [30] are compared when $U/W = 1/2$, $\delta = 0.2$, and $t_{\perp} = 0$. When t_{\perp} is finite, the average sign increases further (not illustrated). We attribute this strange behavior to the action of the host on the cluster, but its actual mathematical justification is still mysterious. Nevertheless, due to the large reduction in the severity of the sign problem, we are able to study the physics at significantly lower temperatures than is possible with FSS!

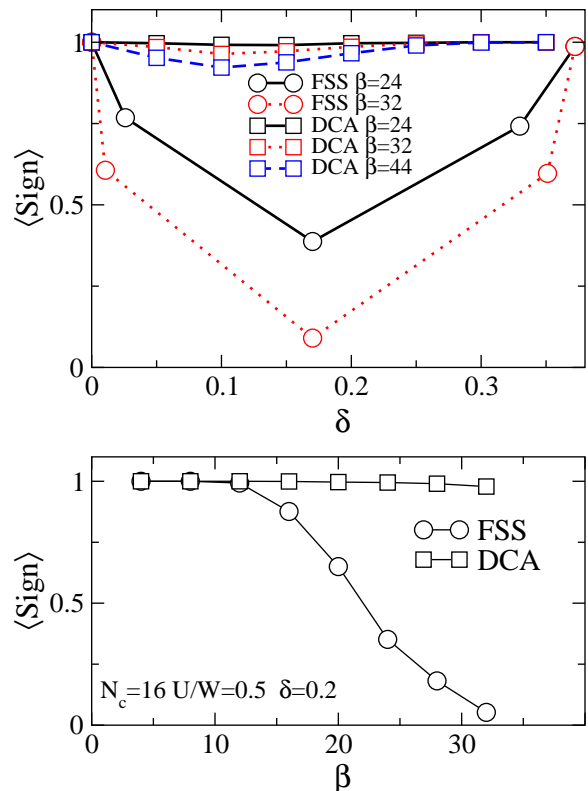


FIG. 15. A comparison of the average sign for the DCA and FS simulations [30] when $U/W = 1/2$, $\delta = 0.2$, $t_{\perp} = 0$.

2. Single-Particle Properties

Much can be learned about the single-particle properties of the system, especially Fermi liquid formation, from studying the momentum distribution function $n(\mathbf{k})$, the single-particle spectra $A(\mathbf{k}, \omega)$ and the single-particle self energy $\Sigma(\mathbf{k}, \omega)$. For a Fermi liquid, the self energy $\Sigma(\mathbf{k}_F, \omega) \sim (1 - 1/Z)\omega - ib\omega^2$ where $b > 0$, $1/Z > 1$ and \mathbf{k}_F is a point on the Fermi surface. The corresponding $A(\mathbf{k}_F, \omega)$ is expected to display a sharp Lorentzian-like peak, and $|\nabla n(\mathbf{k})|$ is also expected to become sharply peaked at the Fermi surface. In each case, these quantities are calculated by first interpolating the cluster self energy onto the lattice \mathbf{k} points.

For example, the gradient of the momentum distribution function is plotted in Fig. 16 when $U = 1$, $\beta = 44$, $\delta = 0.05$ for different values of N_c (this temperature would correspond to roughly room temperature for the cuprates in units where the bare bandwidth $W = 2\text{eV}$). Apparently, at this temperature, there are two Fermi surface features, one centered at $\Gamma = (0, 0)$ and one centered at $M = (\pi, \pi)$. The Fermi surface centered at $\Gamma = (0, 0)$ has roughly the volume expected of non-interacting electrons, so we will call it the electron-like surface and the other hole-like. Note that the hole-like Fermi surface becomes more prevalent, and the peak near $(\pi/2, \pi/2)$ diminishes, as N_c increases. We therefore attribute this behavior to short-ranged correlations.

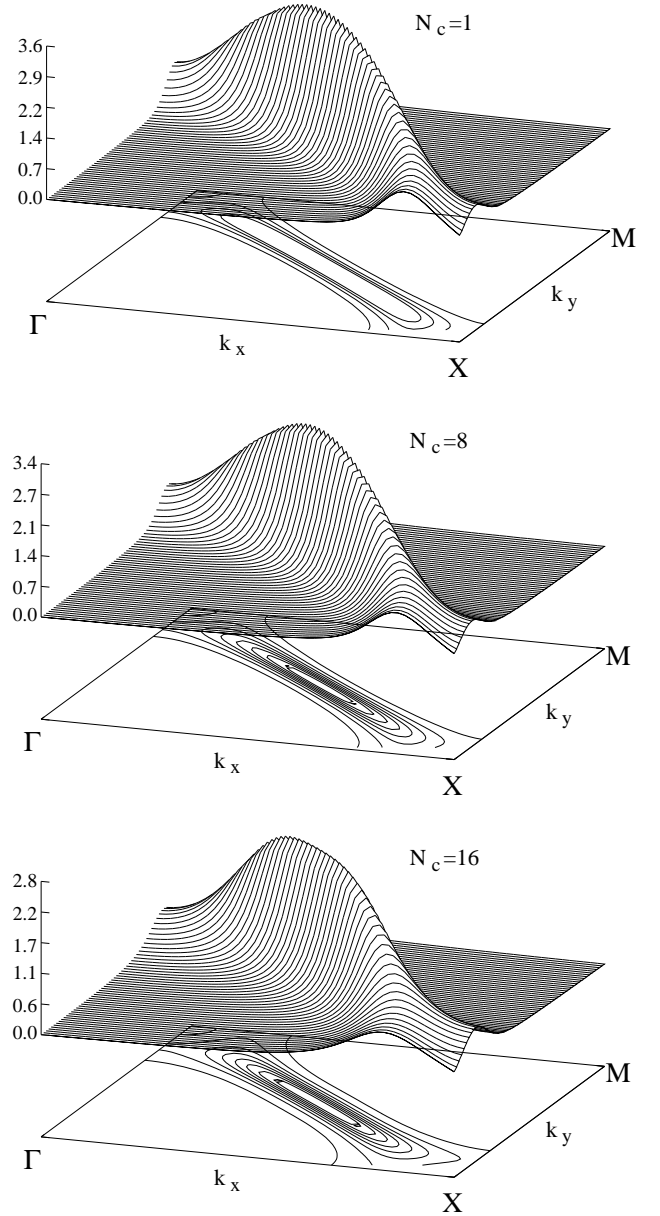


FIG. 16. $|\nabla n(\mathbf{k})|$ versus \mathbf{k} when $U = 1$, $\beta = 44$, $t_{\perp} = 0$ and $\delta = 0.05$ for $N_c = 1, 8$ and 16 .

We can further resolve the different surface features, by investigating the single-particle spectrum $A(\mathbf{k}, \omega)$ as shown in Fig. 17 for $U = 1$, $\beta = 44$, $\delta = 0.05$ and $N_c = 16$. The graph (d) on the upper left of Fig. 17 plots the corresponding location of the maxima of $|\nabla n(\mathbf{k})|$. Along the direction from Γ to M , $A(\mathbf{k}, \omega)$ shows a relatively well defined and symmetric peak at $\omega = 0$ at the location as indicated by the maximum of $|\nabla n(\mathbf{k})|$. The only notable feature is that the peak is a bit better defined for \mathbf{k} closer to the zone center Γ . Along the direction from M to X , the part of the hole-like Fermi surface closest to the X point is resolved. Here the peak in $A(\mathbf{k}, \omega)$ crosses the Fermi surface at roughly the same \mathbf{k} where the peak in $|\nabla n(\mathbf{k})|$ is seen; however, the peak in $A(\mathbf{k}, \omega)$ is broader and is heavily skewed to higher frequencies. Fi-

nally, along the direction from X to Γ , we find very sharp peaks in $A(\mathbf{k}, \omega)$; however, none occur at $\omega = 0$ indicating that there are well defined quasiparticle excitations along this direction, with a small pseudogap, presumably due to the short-ranged order. This pseudogap behavior becomes more pronounced as the temperature is lowered.

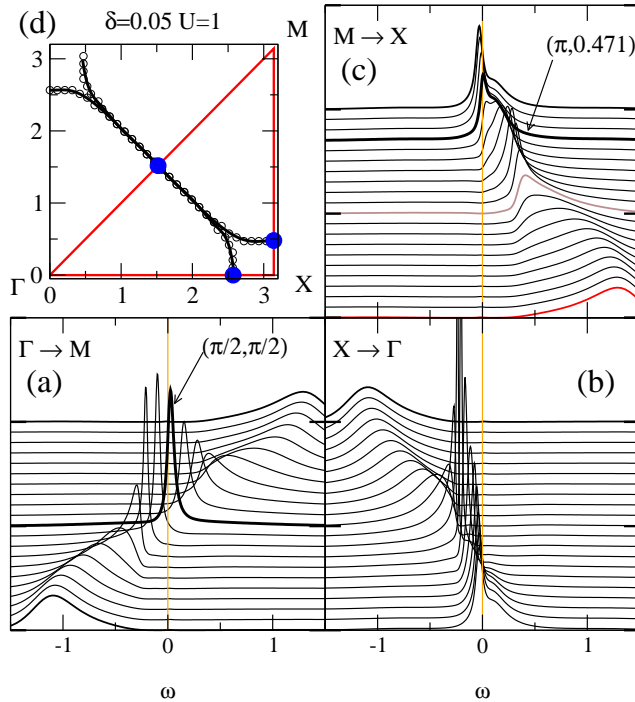


FIG. 17. (a)–(c) The single-particle spectrum $A(\mathbf{k}, \omega)$ for $U = 1$, $\beta = 44$, $\delta = 0.05$, $t_{\perp} = 0$ and $N_c = 16$ along certain high symmetry directions. The arrows and bold lines in Figs. (a) and (c) indicate the spectra which cross the Fermi energy with a peak closest to $\omega = 0$. In (b), no such peak is found which crosses the Fermi energy. (d) the maxima of the $|\nabla n(\mathbf{k})|$ data illustrated in Fig. 16 plotted versus \mathbf{k} .

This can be seen in the density of states, shown in Fig. 18 where the gap is more pronounced. At high temperatures, $\beta = 4$ the Hubbard side bands are apparent at $\omega \approx \pm 1/2$. As the temperature is lowered, a central peak begins to develop. At low temperatures, $\beta \gtrsim 24$ a pseudogap begins to develop.

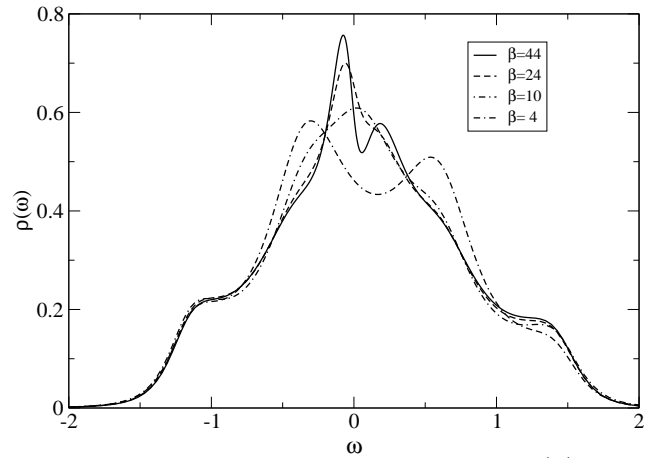


FIG. 18. The single-particle density of states $\rho(\omega)$ when $U = 1$, $\delta = 0.05$, $t_{\perp} = 0$ and $N_c = 16$ for several different values of the inverse temperature β . As the temperature is lowered, $\rho(\omega)$ develops a pseudogap due to the short-ranged antiferromagnetic order.

More can be learned by investigating the self energy directly. In Fig.19, both the real and imaginary parts of the self energy are plotted for the three values of \mathbf{k} indicated by filled circles in Fig. 17(d). The self energy on the part of the Fermi surface along the direction from Γ to M , looks roughly Fermi-liquid like. However, the self energy on the parts of the Fermi surface closest to X have pronounced non-Fermi liquid character, especially at $\mathbf{k} = (\pi, 0.48)$ where the real part displays a minimum and the imaginary part crosses the Fermi energy almost linearly. At $\mathbf{k} = (2.571, 0)$, the real part again displays a minimum, but the imaginary part has an almost Fermi-liquid-like maximum at the Fermi energy, and then once again the scattering rate increases dramatically at higher energies. All of the points close to X share this dramatic asymmetry; that excitations below the Fermi energy are much longer lived than those above. Thus, we expect that the transport from these parts of the Fermi surface would be predominantly hole-like.

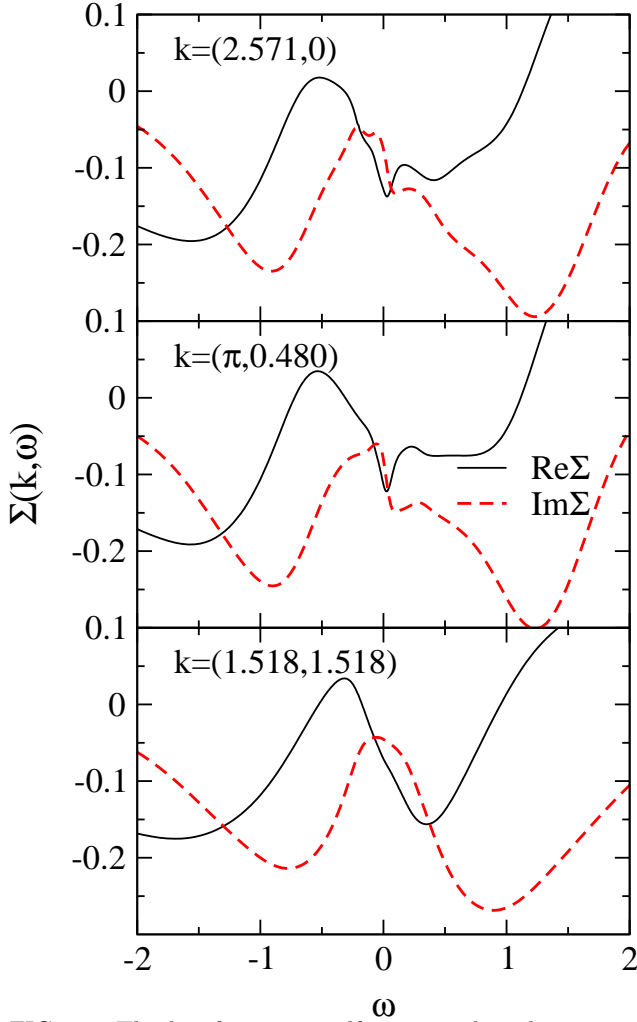


FIG. 19. The low-frequency self energy, plotted versus ω for the three \mathbf{k} -points denoted by filled circles in Fig. 17(d) where the Fermi surface defined by the maxima of $|\nabla n(\mathbf{k})|$ crosses the high symmetry directions.

The non-Fermi liquid features, including the hole-like distortion of the Fermi surface, the anisotropy and non-Fermi liquid features of the self energy, and the pseudogap in the density of states, become more pronounced as N_c increases. Thus, it is reasonable to assume that these features will persist as $N_c \rightarrow \infty$.

3. Superconductivity

We searched for many different types of superconductivity, including s, extended-s, p and d-wave, of both odd and even frequency and we looked for pairing at both the zone center and corner. Only the pairing channels with zero center of mass momentum (zone center) are enhanced as the temperature falls. Of these, only the even-frequency d-wave pair field susceptibility diverges. This is illustrated in Fig. 20 where all of the zone center susceptibilities are plotted versus temperature for $U = 1.5$,

$N_c = 8$ and $\delta = 0.05$.

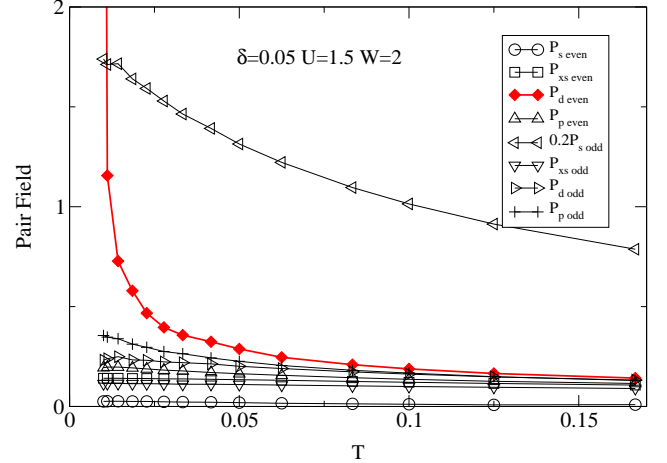


FIG. 20. Various pair field susceptibilities calculated at the zone center and plotted versus temperature for $U = 1.5$, $\delta = 0.05$, $t_{\perp} = 0$, and $N_c = 8$. Pairing is found only in the even-frequency $\mathbf{q} = 0$ d-wave channel.

In contrast to the antiferromagnetic susceptibility which falls as N_c increases, the d-wave pair field susceptibility generally rises with N_c , except at very low temperatures. This is illustrated in Fig. 21. However, for $N_c = 16$ at low T , it falls abruptly when $T \lesssim 0.03$. This behavior is consistent with the lack of superconductivity in the purely two-dimensional model. However, in the inset, we see that a very small interplanar coupling $t_{\perp}/t = 0.2$ causes the susceptibility to continue to rise with decreasing temperature. Thus, perhaps a very small interplanar coupling is able to stabilize the mean-field superconductivity seen in smaller clusters [48,47].

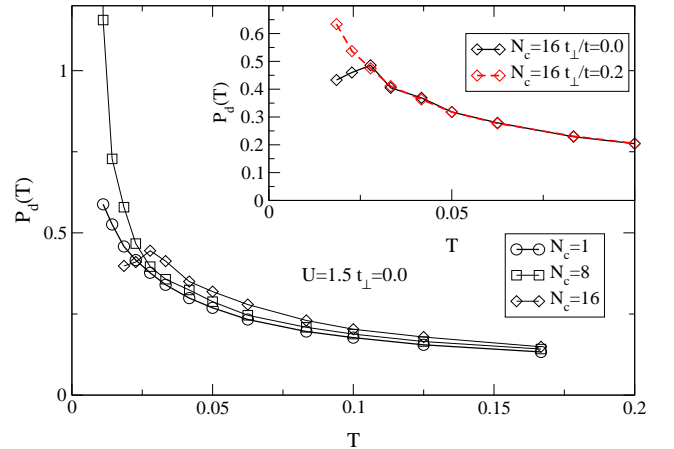


FIG. 21. The d-wave pair field susceptibility versus T for several values of N_c when $U = 1.5$, $\delta = 0.05$ and $t_{\perp}/t = 0.0$. In the inset the d-wave pair field susceptibility is plotted versus T when $N_c = 16$, $U = 1.5$ and $\delta = 0.05$ for $t_{\perp}/t = 0.2$.

VII. SUMMARY

We have presented the algorithmic details of the dynamical cluster approximation. The technique consists of mapping the original lattice problem to a problem involving a finite cluster dynamically coupled to an infinite host. The cluster problem may be solved by a variety of techniques that include the QMC method, the FLEX approximation or the NCA.

An extensive account of a QMC method used to solve the cluster problem was given. Though this algorithm requires significantly greater computer power than the Blawie-Sugar-Scalapino algorithm which is often used for finite systems, it has some advantages. First, it does not show any numerical instability at low temperature; thus, it avoids the time costly matrix factorization step that slows down the BSS algorithm. Second, the algorithm is quite general and can be applied to problems that do not have any explicit Hamiltonian formulation with known parameters. Third, a mean-field coupling to other degrees of freedom may be easily incorporated. Fourth, the minus sign problem is far less severe in DCA simulations. This allows us to study systems at significantly lower temperatures, with stronger interactions, or with larger clusters than can be studied with the BSS algorithm when the sign problem is apparent.

The full DCA algorithm is made of three separate units. In the first unit the coarse-graining of the lattice is performed and the resulting self-consistent cluster problem is solved by the QMC technique. This unit requires the formidable computer power available on massively parallel computers. The second part deals with the calculation of the lattice one and two-particle Green functions from those of the embedded cluster. In the last part the analytical continuation of the imaginary-time Green functions to real frequency Green functions is performed.

In order to illustrate the originality of the DCA technique, we have applied it to the two-dimensional Hubbard model with a small interplanar mean-field coupling.

The DCA method was developed to address some of the shortcomings encountered in the dynamical mean-field theory. The lack of non-local fluctuations in the DMFA leads to incorrect predictions when this method is applied to systems in finite dimension. In particular, we have seen that in violation of the Mermin-Wagner theorem, the DMFA predicts a finite-temperature transition in the two-dimensional Hubbard model. We have shown that in the DCA, this transition is progressively suppressed as the range of the fluctuations (i.e the cluster size) is increased.

We also find that a finite-temperature gap persists well into the weak coupling regime of the half filled model. As the DCA systematically underestimates the gap formation, these conclusions are valid in the limit $N_c \rightarrow \infty$. Since the temperature where the gap opens increases with N_c , while T_N decreases, the Slater mechanism is likely not responsible for the metal-insulator transition in the two

dimensional Hubbard model. The resulting phase diagram is consistent with Anderson's view that the effective Hamiltonian for the 2D Hubbard model at half-filling for all $U > 0$ and $\Delta \gg T$ (where Δ is the gap energy) is the 2D Heisenberg Hamiltonian [49].

We find no evidence for a Kondo peak, or the associated Fermi liquid behavior for the unfrustrated model near half filling. Since this is an essential feature of the DMFA solution of the doped model or the half filled model with $U \lesssim W$, we conclude that the DMFA is a very poor approximation for the two-dimensional model, especially for behavior such as the Mott transition, observed near or at half filling.

When the model is doped, the sign problem becomes significant and will certainly affect the quality of the results. However, the sign problem is significantly less severe than that found in finite size systems, allowing us to explore these model systems at significantly lower temperatures, larger coupling or larger clusters than heretofore possible. In the doped model, we find evidence of non-Fermi liquid behavior even for relatively small values of U/W . This has been observed in the self energy, single particle spectra, and density of states. We also find that the d-wave pair-field susceptibility is divergent for small clusters. A trend that is not present in the DMFA because the method cannot treat non-local order parameters.

Finally, the DCA is a very versatile technique that may be applied to a variety of problems. A straightforward generalization of this algorithm to the periodic Anderson model in two dimensions will allow us to study the physics of the recently discovered two-dimensional heavy fermion systems. In its present form, we have incorporated diagonal disorder in the 2D Hubbard model which will allow us to address the interesting problem of disorder and interaction in two dimensions. A future improvement of the DCA algorithm itself is to insert long range fluctuations in the algorithm which would be treated perturbatively.

Acknowledgments: We wish to thank H. Akhlagpour, N. Blümer, A. Gonis, M. Hettler, H.R. Krishnamurthy, E. Müller-Hartmann, Th. Pruschke, A.N. Tahvildarzadeh, and Y. Wang. We would like to dedicate this paper to E. Müller-Hartmann, on the occasion of his 60th birthday. The QMC code described in this manuscript was developed by MJ and CH in collaboration with A.N. Tahvildarzadeh. We thank Y. Wang for assistance with MPI. This work was supported by NSF grant DMR-0073308 and by the Ohio Supercomputer Center. This research was supported in part by NSF cooperative agreement ACI-9619020 through computing resources provided by the National Partnership for Advanced Computational Infrastructure at the Pittsburgh and San Diego Supercomputer Centers.

- [1] E. Dagotto, Rev. Mod. Phys. **66**, 763 (1994).
- [2] W. Metzner and D. Vollhardt, Phys. Rev. Lett. **62**, 324 (1989).
- [3] E. Müller-Hartmann, Z. Phys. **B 74**, 507–512 (1989).
- [4] T. Pruschke, M. Jarrell and J.K. Freericks, Adv. in Phys. **42**, 187 (1995).
- [5] A. Georges, G. Kotliar, W. Krauth and M.J. Rozenberg, Rev. Mod. Phys. **68**, 13 (1996).
- [6] The problems encountered in forming cluster corrections to the DMFA are the same as those encountered in the coherent potential approximation (CPA) for disordered systems. For a detailed discussion of earlier work on the inclusion of non-local corrections to the CPA see A. Gonis, *Green functions for ordered and disordered systems*, in the series *Studies in Mathematical Physics* Eds. E. van Groesen and E. M. DeJager, (North Holland, Amsterdam, 1992).
- [7] M.H. Hettler, A.N. Tahvildar-Zadeh, M. Jarrell, T. Pruschke, and H.R. Krishnamurthy, Phys. Rev. **B 58**, 7475 (1998).
- [8] M. H. Hettler, M. Mukherjee, M. Jarrell, and H.R. Krishnamurthy, Phys. Rev. **B 61**, 12739 (2000).
- [9] Th. Maier, M. Jarrell, Th. Pruschke and J. Keller, Eur. Phys. J. **B 13**, 613 (2000).
- [10] J.E. Hirsch and R.M. Fye, Phys. Rev. Lett. **56**, 2521 (1986).
- [11] N.E. Bickers, D.J. Scalapino, and S.R. White, Phys. Rev. Lett., **62**, 961 (1989).
- [12] N.E. Bickers, D.L. Cox, and J.W. Wilkins, Phys. Rev. **B36** 2036 (1987).
- [13] C. Huscroft, M. Jarrell, Th. Maier, S. Moukouri, A.N. Tahvildarzadeh, Phys. Rev. Lett., **86**, 3691 (2001).
- [14] S. Moukouri, C. Huscroft, and M. Jarrell, to appear in *Computer Simulations in Condensed Matter Physics VII*, edited by D.P. Landau, K.K. Mon, and H.B. Schuttler (Springer-Verlag, Heidelberg, Berlin, 2000).
- [15] M. Jarrell and J.E. Gubernatis, Phys. Rep. **269**, 135 (1996).
- [16] S. Moukouri and M. Jarrell, preprint cond-mat/0011247.
- [17] G. Treglia, F. Ducastelle and D. Spanjaard, Phys. Rev. **B 21**, 3729 (1980).
- [18] Y. Kuramoto, in *Theory of Heavy Fermions and Valence Fluctuations*, edited by T. Kasuya and T. Saso, Springer Ser. Solid State Sci., Vol. **62**, p. 152 (Springer, Berlin, 1985).; C. Kim, Y. Kuramoto and T. Kasuya, J. Phys. Soc. Jpn., **59** 2414 (1990) .
- [19] A.A. Abrikosov, L.P. Gorkov, I.E. Dzyalishinski, *Methods of Quantum Field Theory in Statistical Physics*, (Dover, New York, 1975).
- [20] K. Aryanpour, M.H. Hettler and M. Jarrell, in preparation.
- [21] P.G.J. van Dongen, Phys. Rev. **B 50**, 14016 (1994).
- [22] A. Schiller and K. Ingersent, Phys. Rev. Lett. **75**, 113, (1995).
- [23] V. Zlatić and B. Horvatić, Sol. St. Comm. **75**, 263 (1990).
- [24] M. Jarrell, Phys. Rev. Lett. **69**, 168(1992)
- [25] G. Baym and L.P. Kadanoff, Phys. Rev. **124**, 287, (1961).
- [26] R. Blankenbecler, D.J. Scalapino, and R.L. Sugar, Phys. Rev. **D 24**, 2278 (1981).
- [27] J.E. Hirsch, Phys. Rev. **B 28**, 4059 (1983).
- [28] J. W. Negele, H. Orland, *Quantum Many-Particle Systems*, (Addison-Wesley Publishing Co., 1988).
- [29] T. Maier, M. Jarrell, and Th. Pruschke, Phys. Rev. Lett. **86**, 3691.
- [30] S.R. White, D.J. Scalapino, R.L. Sugar, E.Y. Loh, J.E. Gubernatis, and R.T. Scalettar, Phys. Rev. **B 40**, 506 (1989).
- [31] E. Y. Loh and J.E. Gubernatis, in *Electronic Phase Transitions*, edited by W. Hanke and Y.-V. Kopaev, (Elsevier, New York, 1992), chap. 4.
- [32] M. Jarrell, H. Akhlaghpour and T. Pruschke, in *Quantum Monte Carlo Methods in Condensed Matter Physics*, Eds. M. Suzuki (World Scientific, Singapore, 1993), p. 221–234, 1993.
- [33] G. Engeln-Müllges and F. Uhlig, *Numerical Recipes with Fortran*, (Springer, Berlin, 1996).
- [34] J. Deisz, private communication.
- [35] See <http://www.netlib.org>.
- [36] *Numerical Recipes in Fortran 77*, Second Edition, W.H. Press, S.A. Teukolsky, W.T. Betterling, and B.P. Flannery, (Cambridge University Press, 1997), page 364.
- [37] L.B. Ioffe and A.J. Millis, Science **285** 1241 (1999); O.K. Andersen *et al.*, Phys. Rev. **B 49**, 4145 (1994).
- [38] J. E. Hirsch, Phys. Rev. **31**, 4403 (1985).
- [39] M. Vekic and S.R. White, Phys. Rev. **B 47**, 1160 (1993).
- [40] E.H. Lieb and F.Y. Wu, Phys. Rev. Lett. **20**, 1445 (1968).
- [41] It is possible that close to the transition ($T \rightarrow T_N$) γ will return to its mean field value of one.
- [42] E.Y. Loh, J.E. Gubernatis, R.T. Scalettar, S.R. White, D.J. Scalapino, and R.L. Sugar, Phys. Rev. **B 41**, 9301 (1990).
- [43] Shiwei Zhang, J. Carlson and J.E. Gubernatis, Phys. Rev. Lett. **74**, 3652 (1995).
- [44] Shiwei Zhang, Phys. Rev. Lett. **83**, 2777 (1999).
- [45] S. Sorella, cond-mat/9803107; S. Sorella and L. Capriotti, cond-mat/9902211.
- [46] Shailesh Chandrasekharan and UweJens Wiese, Phys. Rev. Lett. **83** 3116 (1999).
- [47] M. Jarrell, Th. Maier, M. H. Hettler, A.N. Tahvildarzadeh, preprint cond-mat/0011282.
- [48] Th. Maier, M. Jarrell, Th. Pruschke, J. Keller, Phys. Rev. Lett. **85**, 1524 (2000).
- [49] P.W. Anderson, Phys. Rev. Lett. **64**, 1839 (1990); **65**, 2306 (1990).